Experimental Demonstration of a Gravitational Wave Detector Configuration Below the Shot Noise Limit

Kirk McKenzie
20 June 2002

Supervisors
Prof. David McClelland
Dr Daniel Shaddock
Dr Ping Koy Lam
Dr Ben Buchler

A thesis submitted as partial fulfillment of the requirements
for the degree of Bachelor of Science (Honours)
at the Australian National University

Declaration

This thesis is an account of the research undertaken with the supervision of Prof. David McClelland and Dr Daniel Shaddock in the Gravitational Waves Detection Group and Dr Ping Koy Lam and Dr Ben Buchler in the Quantum Optics Group at the Department of Physics between July 2001 and June 2002. I declare that all work presented is my own, unless otherwise stated.

Kirk McKenzie 20 June 2002

Acknowledgments

I would sincerely like to thank the many people that have supported me and shared friendship and fun with me throughout the last year.

I feel privileged to have had fantastic supervisors while performing the research presented in this thesis: Prof. David McClelland, Dr. Daniel Shaddock, Dr. Ping Koy Lam and Dr. Ben Buchler.

I would like to thank David for the opportunity to carry out this research and for the honours scholarship. David always made time for useful discussions. His ability to simultaneously view the intricacies of the research and maintain a view of the 'big picture' has been invaluable.

I thank Dan for all his help throughout the year and for persuading me to choose this research. Dan has passed on lots of his seemingly endless knowledge through countless whiteboard sessions. Dan was a great help in both the development of the theory behind the experiment and in the lab.

I would like to thank Ping Koy for the opportunity to perform this research and for the honours scholarship. Ping Koy has helped in many discussions, providing insight and clarity into many areas.

I thank Ben for the all the help throughout the year. Without Ben the work presented here would not have been possible. Ben built the squeezer used in the experiment and gave great help in the lab. I have had many good discussions and learnt so much from him.

In no specific order, I would like to thank the following people. Bram for being a great group leader (organizing all of the roosters) and for lending me his laptop; Glenn for his constant humor; Conor for helping me string a few decent sentences together; Ben. S for sharing his office with me; Benedict for valuable support; Mal for useful discussion and positive attitude; Simon for the all fun shared, including writing the thesis, driving me to school and the ultimate game; John, Nick, Jess and Cameron; Thanks Cameron for teaching me about the physics of coffee cooling down; Craig for being a great honours coordinator; Warrick for insight to the various ways one can squeezed light; Thanks to Andrew for sharing his office; Thanks to all my other colleagues at the physics department; Thanks to Zeta for organizing various things; Thanks to all of the other honours students. In order of closeness to GW; Conor, Nicolai, Aska, Simon, Doug, Tim, Anne, Annabele, Phil and Taira.

Thanks Ben, David, Ping Koy, Dan, Mal, Conor, and Dad for all the proof reading of this thesis. Naturally, I take responsability for the remaining mistakes.

Finally, I would like to thank Gran, Angie, Zoe, Dave and Lee for missing me. Thanks Mum, Dad and Hugh for helping me with everything. And thankyou Ella for your love and for being there for me.

Abstract

Unprecedented sensitivity of measurement is required to detect gravitational waves. Although the first generation of interferometric gravitational wave detectors are the most sensitive devices ever built, it is expected they will not be sensitive enough to regularly detect gravitational waves.

The precision of the optical measurement used in gravitational wave detectors is ultimately limited by the quantum mechanical fluctuations of the light, called quantum noise. The first generation of interferometric gravitational wave detectors have reached the quantum noise limit at some frequencies. Second generation interferometric gravitational wave detectors are expected to be limited by quantum noise across most of the detection frequency band.

This thesis presents the first experimental demonstration of a gravitational wave detector configuration with sensitivity below the quantum noise limit. The configuration demonstrated is a power recycled Michelson interferometer with the addition of squeezed light. The control of the configuration and the method for injection of squeezed light are compatible with current gravitational wave detectors. A model for the configuration is derived using linearized operators for the optical fields.

The results obtained demonstrate the improvement below the shot noise limit using squeezed light, and the interaction of power recycling with squeezed light is investigated. The predictions made using the model show excellent agrement with the experimental results. The entire system maintains stable lock for long periods.

Contents

Acknowledgments i

Summary of Thesis iii

1 Introduction 1
- 1.1 Gravitational waves . . . 1
- 1.2 Why detect gravitational waves? . . . 2
- 1.3 The direct detection of gravitational waves . . . 3
- 1.4 Noise sources in a gravitational wave detector . . . 4
  - 1.4.1 Shot noise . . . 5
  - 1.4.2 Radiation pressure noise . . . 5
  - 1.4.3 Thermal noise . . . 5
  - 1.4.4 Seismic noise . . . 5
- 1.5 Advanced interferometer configurations . . . 5
  - 1.5.1 Power recycling . . . 6
  - 1.5.2 Storage time . . . 6
  - 1.5.3 Arm cavities . . . 7
  - 1.5.4 Signal recycling . . . 7
  - 1.5.5 Current long baseline gravitational wave detectors . . . 7
- 1.6 Motivation and previous work . . . 7
- 1.7 Overview of the experiment . . . 8
- 1.8 Overview of the thesis . . . 8

2 Quantum Noise and Squeezing 11
- 2.1 Overview . . . 11
- 2.2 The Heisenberg uncertainty principle . . . 11
- 2.3 States of light . . . 12
  - 2.3.1 The coherent state . . . 12
  - 2.3.2 The vacuum state . . . 13
  - 2.3.3 The squeezed state . . . 13
- 2.4 Linearization of the operators . . . 14
- 2.5 The production of squeezed light . . . 16
  - 2.5.1 Second harmonic generation . . . 16
  - 2.5.2 Squeezing from a optical parametric amplifier . . . 17
- 2.6 Summary . . . 17

3 Interferometer Control and Detection Theory 19
- 3.1 Overview . . . 19
- 3.2 Introduction to control . . . 19
- 3.3 Phase and amplitude modulation . . . 19
- 3.4 The Fabry-Perot cavity . . . 21

3.5 Interaction of PM with an optical cavity . . . 22
3.6 Locking Techniques . . . 22
3.6.1 Pound Drever Hall locking . . . 22
3.6.2 Offset locking . . . 23
3.7 Detection theory . . . 25
3.7.1 Direct detection . . . 25
3.7.2 Standard Homodyne . . . 26
3.7.3 The measurement of squeezing . . . 28
3.7.4 The Local oscillator in gravitational wave detectors . . . 28
3.8 Inefficient measurements . . . 28
3.8.1 Mode mismatch in homodyne . . . 29
3.8.2 Electronic noise . . . 30
3.9 Chapter summary . . . 30

4 Theory of a Power Recycled Michelson Interferometer with Squeezed Light 31
4.1 Overview . . . 31
4.2 Equivalent optical circuits . . . 31
4.2.1 The Michelson interferometer . . . 31
4.3 Power recycled Michelson with Squeezing . . . 32
4.3.1 Fields in the interferometer . . . 33
4.3.2 The transfer functions of the interferometer . . . 34
4.3.3 The field at the output of the interferometer . . . 36
4.4 Chapter summary . . . 38

5 The Experiment 39
5.1 Overview . . . 39
5.2 The laser . . . 39
5.3 Preparation of the light . . . 39
5.3.1 The modecleaner . . . 40
5.3.2 Mode-matching . . . 40
5.3.3 Polarization optics . . . 41
5.4 Experimental techniques . . . 41
5.4.1 Signal generation . . . 41
5.4.2 Squeezed light injection optics . . . 42
5.5 Optical Layout . . . 43
5.5.1 Discussion of the optical layout . . . 43
5.5.2 The optical layout of the squeezer . . . 44
5.6 Control . . . 45
5.6.1 Control of power recycled Michelson with squeezing . . . 46
5.6.2 Gain estimates . . . 47
5.6.3 Control of the squeezer . . . 47
5.7 Electronic equipment . . . 48
5.7.1 Total experiment . . . 49
5.8 Chapter summary . . . 49

6 Experimental Results **51**
6.1 Initial parameters . . . 51
6.1.1 The carrier noise measurement . . . 51
6.1.2 Measurement of the squeezed light . . . 52
6.1.3 Signal . . . 53
6.2 Power recycling factor and losses . . . 54
6.2.1 Power recycling factor . . . 54
6.2.2 PRM intra cavity losses . . . 55
6.2.3 Injection optics loss . . . 56
6.3 Power recycled Michelson with squeezed light . . . 56
6.3.1 Noise out of the PRM . . . 56
6.3.2 Characterization of the system . . . 57
6.3.3 PRM with squeezed light locking performance . . . 58
6.3.4 Comparison of different power mirror reflectivities . . . 59
6.4 Summary of results . . . 60

7 Conclusion and further work **61**
7.1 Further Work . . . 61

Bibliography **63**

A Derivation of Transfer functions **67**

B Model MatLab code **69**
B.1 Code for PRM with squeezed light . . . 69
B.2 transfer functions for PRM with squeezed light . . . 71

C MatLab code for gain estimates **73**
C.1 Main file . . . 73
C.2 Sub file . . . 76

D Control Equipment **77**
D.1 Servo frequency response . . . 77
D.2 PZT response . . . 77

Chapter 1

Introduction

Gravitational radiation [1] is predicted by Einstein's General Theory of Relativity [2]. This theory suggests that masses curve space-time. If space-time can be curved it is flexible and allows wave-like solutions called gravitational waves.

The endeavour to detect gravitational waves is one of the most challenging areas in science and engineering [3]. Tremendous efforts have been applied to solving both the technical and fundamental problems, drawing many different fields of physics together.

The fundamental limit to the sensitivity of any measurement is imposed by *quantum noise* [4], as described by the Heisenberg uncertainty principle. The quantum noise limit has been recognized in interferometric gravitational wave detectors for many years. However, up until recently quantum noise has not limited gravitational wave detector's sensitivity. The first theoretical proposal to surpass the shot noise limit was published by Caves in 1981 [5]. Many other theoretical investigations have been published since including [6–8], but until now quantum noise reduction in a gravitational wave detector configuration had not been experimentally achieved. This thesis presents the first experimental demonstration of an improvement to gravitational wave detection sensitivity using a technique that allows quantum noise reduction.

1.1 Gravitational waves

Gravitational waves can be conceptualized by analogy with familiar electromagnetic waves [9]. Like electromagnetic waves, gravitational waves propagate at the speed of light. Electromagnetic waves propagate through space-time, whereas gravitational waves propagate as ripples in space-time. The emission of electromagnetic waves is caused by accelerating electric charges. Similarly, gravitational waves are emitted by accelerating masses. The lowest mode of oscillation for electromagnetic waves is dipole. This is unlike gravitational waves, where the lowest mode of oscillation for is quadrupole [10]. The difference arises because electric charge has both positive and negative values whereas mass is always positive.

To assist in the understanding of gravitational waves, their effect on a region of space-time is described. Figure 1.1 shows the effect of a quadrupole gravitational wave on a ring of test masses with each frame advanced by one quarter of a period. The gravitational wave, propagating into the page, is seen to stretch the ring in one direction and squash it orthogonally. This is because of perturbations of the space-time between the masses. This is the effect of the h_+ polarization wave. The orthogonal polarization, $h_\times$, has the same effect, only with the axes of the distortions rotated by 45^o. The strength of a gravitational wave is measured by the fractional length change it induces,

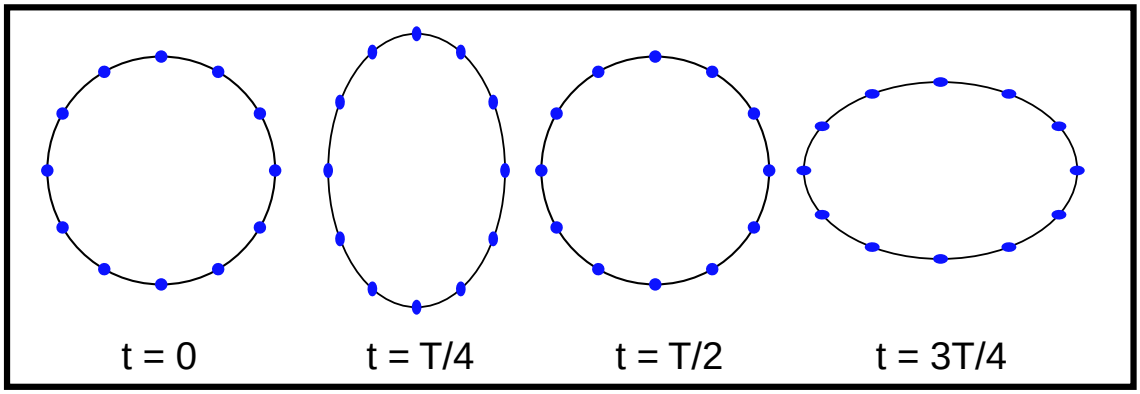

Figure 1.1: The effect of a passing gravitational wave on a ring of test masses floating in space shown at 1/4 period intervals.

$$\frac{\delta L}{L} = \frac{h}{2} \tag{1.1}$$

here δL is the change in length, L is the unperturbed length, and h is the strain. The largest common events are predicted to have $h \sim 10^{-21}$ and occur several times per year. This strain, is equivalent to a length change (δL) of a hairs width in a length (L) of the Earth to the nearest extra solar star, Proxima Centuri, 4.3 light years away. The sensitivity required to measure such an effect on a terrestrial scale is extraordinary.

1.2 Why detect gravitational waves?

The direct detection of gravitational waves will have many significant outcomes. Data taken in the previously unmeasured strong gravity limit will enable a rigorous examination of General Relativity. Another outcome is the potential it could offer for a new type of astronomy. Astronomy has used electromagnetic waves for thousands of years to improve our understanding of the universe. Recently, many parts of the previously unmeasured electromagnetic spectrum have been detected, due to technological advances, opening new windows for astrophysical study. However, all electromagnetic measurements are limited by both absorption in matter and the lack of emission, locking away information from the densest and darkest areas of space. Gravitational waves interact so weakly with matter that they are not absorbed. This allows many astrophysical objects to be studied that were previously invisible in the electromagnetic spectrum.

An example of an expected gravitational wave source is the collapse of binary neutron star systems. The large masses (~ 2 solar masses) and small radii ($\sim 10\mathrm{km}$) involved, makes them a prime candidate for strong, high frequency gravitational wave emission. The system will lose orbital angular momentum in the form of gravitational radiation, emitted at twice the orbital frequency, and the binary neutron stars fall into ever closer orbits. This in turn produces larger amplitude radiation at increasing frequency. The separation of the two neutron stars decreases until they eventually coalesce. The coalescence releases a final burst of gravitational radiation. Much of the physics of the coalescence is

unknown, and the detection of gravitational waves will shed new light onto the dynamics of this process.

1.3 The direct detection of gravitational waves

The direct detection of gravitational waves is yet to be achieved, due to the unprecedented sensitivity of the measurements required. However, indirect evidence of gravitational waves was obtained over ten years ago by Hulse and Taylor [11]. They studied the orbital period of the binary neutron star system PSR 1913+16 [12] for more than twenty years and showed it to be decreasing. This decrease in period matched the rate predicted by the General Theory of Relativity if the angular momentum was lost in the form of gravitational waves. This work won Hulse and Taylor the Nobel Prize in 1993.

Laser interferometry is the most promising technique for gravitational wave detection. Long baseline interferometers, between 3 and 4km in length, offer high sensitivity across a broad frequency range of 10 Hz to 10 kHz. The standard configuration of these interferometers is an advanced form of the Michelson interferometer, referred to hereafter as a Michelson.

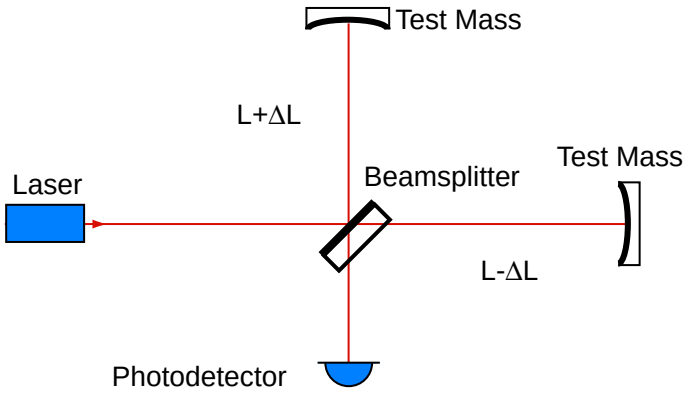

Figure 1.2: Layout of the Michelson interferometer.

A diagram of a Michelson is shown in figure 1.2. The laser light injected into the interferometer is divided into the two arms by the beamsplitter. The field in each arm propagates to the end mirrors (called the test masses) then returns to the beamsplitter. The fields interfere on the beamsplitter, each with a phase shift determined by the path length travelled. The interference condition is dependent on the phase difference between the two fields. This interference determines the amount of light that is transmitted to the output of the interferometer or reflected back toward the laser. The light that is transmitted to the output is detected by a photodetector.

The transmitted and reflected fields are derived as follows. The average length of the arms is defined to be L and difference in length to be ΔL, so that the length of one arm is $L + \Delta L$ and the length of the other is $L - \Delta L$. For incident electric field α_{in}, the electric field at the output, α_{out}, and reflected back towards the laser α_{ref}, are given by,

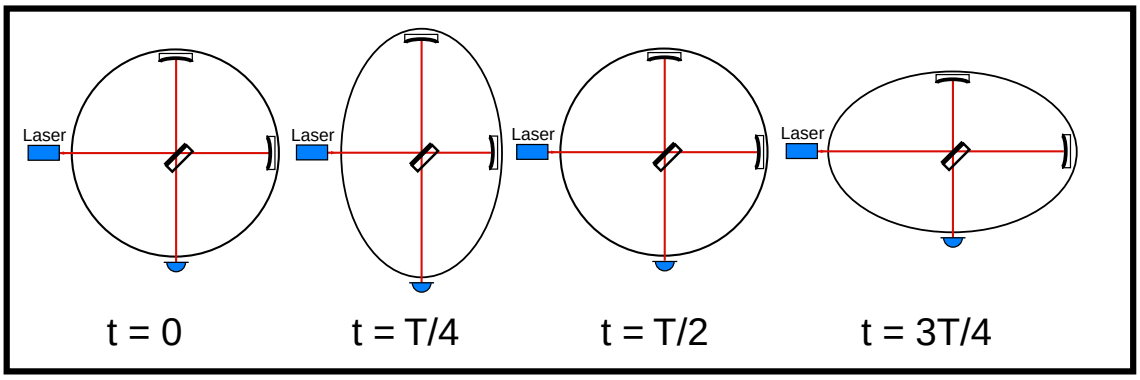

Figure 1.3: The effect of a passing gravitational wave on a Michelson interferometer.

$$\alpha_{out} = \alpha_{in} \sin(2\omega\Delta L/c) \mathrm{e}^{2i\omega L/c} \tag{1.2}$$

$$\alpha_{ref} = \alpha_{in} \cos(2\omega\Delta L/c) \mathrm{e}^{2i\omega L/c} \tag{1.3}$$

where the laser angular frequency is ω and c is the speed of light. Both the reflected and transmitted fields have a common phase shift due to the average length of the arms and a sinusoidally varying term due to the difference in arm length. The common phase shift can be factored out of these equations. It can be seen that the interference condition, and thus the output, is determined only by the arm length difference. The differential phase is defined as,

$$\phi = 2\omega\Delta L/c \tag{1.4}$$

Gravitational wave detectors operate on a dark fringe, with $\phi = 0$, where the fields interfere destructively towards the output. The best signal to noise ratio occurs at a dark fringe. Also, a dark fringe is preferable since current photodetectors cannot deal with the high powers used in modern the interferometers.

The effect of a gravitational wave on a Michelson is the same as the effect on the ring of particles shown in figure 1.1. The test masses of the ring are replaced by the end mirrors of the Michelson, as shown in figure 1.3. A passing gravitational wave will shorten one arm and lengthen the other. This modulates differential phase, ϕ, and thus the interference condition, thereby creating the signal. The signal can be measured at the output of the interferometer in the absence of noise.

1.4 Noise sources in a gravitational wave detector

To detect a gravitational wave signal, the noise on the output must be reduced to unprecedented levels. The sensitivity of current interferometric gravitational wave detectors is limited by three major noise sources: quantum noise of the electromagnetic field in the interferometer, thermal noise in the mirrors and suspension, and seismic noise.

1.4.1 Shot noise

Shot noise arises due to the quantum mechanical fluctuations in the phase quadrature of the electromagnetic field. The sensitivity of first generation detectors are shot noise limited above a few hundred Hertz. Since the gravitational wave signal is also in the phase quadrature, shot noise limits the sensitivity. The shot noise limited signal-to-noise ratio scales inversely with power in the interferometer arms,

$$SNR_S \propto \frac{1}{\sqrt{P}} \tag{1.5}$$

Thus shot noise can be reduced by increasing the power in the interferometer. Shot noise is completely described in chapter 2.

1.4.2 Radiation pressure noise

Radiation pressure noise arises from the quantum mechanical fluctuations in the amplitude quadrature of the electromagnetic field. The second generation detectors are expected to be limited by radiation pressure noise at frequencies below a few hundred Hertz. Radiation pressure noise occurs as a result of the "graininess" of light. For a balanced (50:50 ratio) beamsplitter there will be slightly different numbers of photons in each arm, which impart different momentum kicks on the end mirrors. This couples into phase fluctuations on the light, limiting the sensitivity of the Michelson. The radiation pressure limited signal-to-noise scales with the square root of the power in the arms,

$$SNR_{RP} \propto \sqrt{P} \tag{1.6}$$

Thus radiation pressure noise becomes significant when high powers are used.

1.4.3 Thermal noise

Thermal noise is expected to dominate the sensitivity of first generation detectors between a few tens and hundreds of Hertz. The source of thermal noise is from three main areas: pendulum modes of the suspension of the mirrors, the internal modes of the mirrors and the violin modes in the suspension wires. Each of these results in uncorrelated displacement of the end mirrors, which again limits the sensitivity of the interferometer.

1.4.4 Seismic noise

Seismic noise limits the sensitivity of first generation detectors below ten Hertz. It comes from a lack of complete isolation of the mirrors from seismic activity.

1.5 Advanced interferometer configurations

Advanced gravitational wave interferometer configurations are used to improve the sensitivity of gravitational wave detectors. Although there are many technical difficulties introduced the improvements in sensitivity are crucial. The important concepts and configurations that are involved in gaining these improvements are introduced in this section.

1.5.1 Power recycling

All current and planned gravitational wave detector interferometers use power recycling [13]. As the operating condition of the Michelson interferometer is a dark fringe, all of the light entering the interferometer exits back toward the laser. This light can be recycled back into the interferometer via a mirror placed in front of the Michelson. This is shown in the figure 1.4(a). This 'power mirror' forms a cavity, with the Michelson acting as the other mirror.

The circulating power can be significantly increased, which reduces shot noise. The reflectivity of the power recycling mirror is chosen to maximize circulating power. This condition is satisfied when the cavity is impedance matched, i.e. when the transmission of the power recycling mirror is equal to the round trip loss of the cavity. The power increase comes at the expense of an extra degree of freedom to control to keep the cavity on resonance.

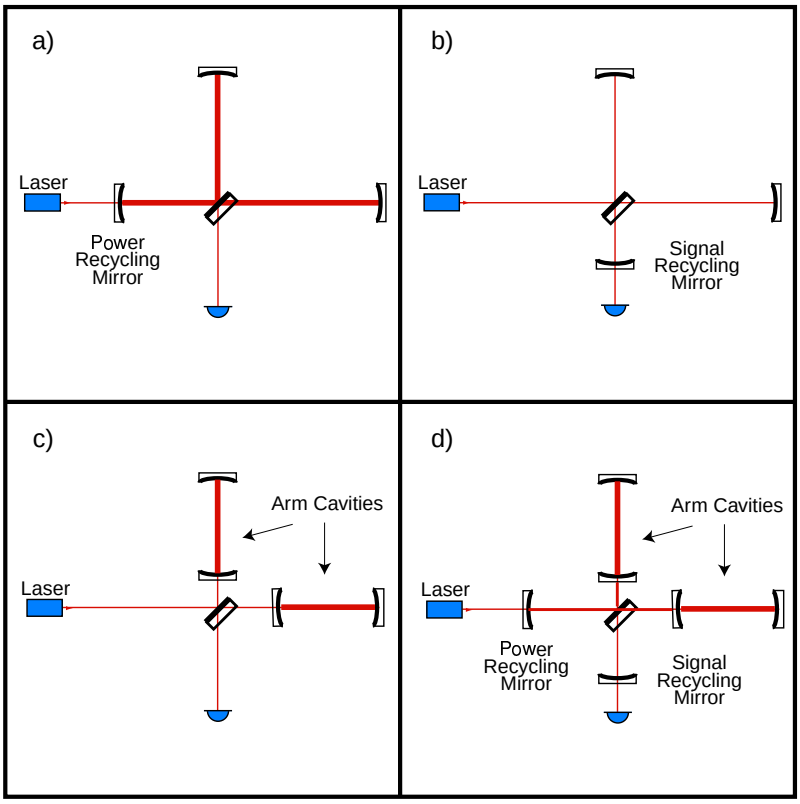

Figure 1.4: Advanced configurations for gravitational wave detection. a) Power recycling, b) Signal recycling, c) Arm cavities and d) Dual recycling with arm cavities

1.5.2 Storage time

To obtain the maximum phase shift from a gravitational wave, the light storage time must be optimized. The light in each arm should have round trip time equal to half the period of the gravitational wave. If the time is shorter and the maximum phase shift will not be imparted on the light, any more and the phase shift will be 'undone'. As an example, the optimal storage time for a 100 Hz gravitational wave signal is 5 ms. Light travels 1500 km

in 5 ms requiring a Michelson arms of half that length, 750 km. Building arm length of this order in ultra high vacuum, and controlling the diffraction of light over this distance is ridiculous. A solution is to fold [10] the interferometer arms, using many bounces to obtain the optimal storage time. Current detectors use Fabry-Perot [14] cavities to fold the light.

1.5.3 Arm cavities

Arm cavities in the gravitational wave detector are single ported Fabry-Perot cavities, as shown in figure 1.4 (c). The storage time is proportional to the linewidth, determined by the length of the cavity and the front mirror reflectivity (since the back mirror is always 100% reflective). The fields resonating in a Fabry Perot cavity overlap spatially and therefore display interference properties. Arm cavities overcome diffraction problems and minimize the size of mirrors needed. They store power, thus reducing shot noise without the need for an increase in laser power. These advantages come at the expense of introducing an extra length degree of freedom for each arm that requires active control.

1.5.4 Signal recycling

The signal recycling mirror is placed at the dark port of the interferometer as shown in figure 1.4 (b). It reflects the signal exiting the Michelson back in, creating a cavity with the Michelson called the signal recycling cavity. The signal reflected back into the interferometer adds coherently with a new signal still being produced. This increases the sensitivity of the detector inside the linewidth of the signal recycling cavity, at the expense of deceased sensitivity outside the bandwidth of the cavity. The detector peak frequency can be adjusted by changing the length of the cavity, whilst the bandwidth can be varied by changing the reflectivity of the signal recycling mirror. The improvement to sensitivity and versatility comes at the expense of yet another degree of freedom needed to be controlled. Some current and all next generation detectors will use signal recycling.

1.5.5 Current long baseline gravitational wave detectors

There are currently four gravitational wave interferometric detectors in the world. The configuration for three of the four is a power recycled Michelson with arm cavities. These detectors are LIGO [15] (in USA), VIRGO [16] (in France) and TAMA [17] (in Japan). Only GEO600 in Germany [18] uses power and signal recycling without arm cavities.

The next generation detectors, such as Advanced LIGO [19], are expected to use resonant sideband extraction (RSE) [20], the configuration shown in figure 1.4 d). RSE is a slight variation on dual recycling with arm cavities.

1.6 Motivation and previous work

The first generation of interferometric gravitational wave detectors are expected to begin taking data in 2002. Although they will be the most sensitive devices ever built, they are predicted to detect only large, infrequent gravitational events. To regularly detect sources, and thereby allow comparison with astrophysical models, a factor of ten improvement in sensitivity is required. The second generation of detectors are expected to reach this goal. Early predictions are that they will be limited by quantum noise over

most of the gravitational wave signal frequency band (10Hz to 1000Hz) [19]. This has sparked an explosion in theoretical papers on the application of quantum optical techniques to surpass these quantum limits in laser interferometry. Included in these is: the use of squeezed light states [8] building on the simple proposal by Caves; What makes these theoretical proposals even more exciting is the fact that the experimental field of generating non-classical light states has reached maturity. From the landmark experiment of Slusher *et al.* [21] in the 1985 in which 0.3dB of quantum noise suppression was measured, bench-top squeezing experiments can now routinely produce over 7dB of quantum noise suppression [22]. A combination of current squeezing technology with the high power and high stability of GW detection laser and optical systems now makes 10dB of squeezing a realistic goal [8].

Despite the potential for squeezing to improve interferometric sensitivity, to date there has been no experimental demonstration of squeezing applied to an interferometer bearing any resemblance to a GW detector. Squeezing enhanced performance has been demonstrated in other interferometers, such as the Mach-Zehnder [23] and polarimeter [24]. None of these experiments employed a Michelson configuration; used light recycling techniques; or utilized a signal readout scheme compatible with an advanced GW detector. Theoretical analysis of Gea-Banachloche *et al.* [6] suggested that squeezing is broadly compatible with recycling techniques. However, the difficulty in devising a readout and control scheme compatible with both squeezing and light recycling has, until now, prevented any definitive demonstration.

1.7 Overview of the experiment

A power recycled Michelson (PRM) with locked optical squeezing injected into the unused port of the beamsplitter is experimentally demonstrated. The squeezing is provided by an optical parametric amplifier (OPA). The laser system, configuration, control and readout system used are all compatible with advanced GW detector proposals. The entire system maintains lock for long periods and we measured a signal with noise below the shot noise limit (SNL). The interaction of power recycling and squeezing is investigated.

A paper has been published on the topic of this research.

· K. McKenzie, D. A. Shaddock, D. E. McClelland, B. C. Buchler and P. K. Lam,
"Experimental demonstration of a squeezing enhanced power recycled Michelson interferometer for gravitational wave detection"
Phys. Rev. Lett. **88**, 231102 (2002)

1.8 Overview of the thesis

In this chapter Gravitational waves and their detection has been introduced. Previous work in the field has been presented leading to the motivation behind this work.

In chapter 2 the theory of quantum noise and squeezing are introduced. The method of linearization of the operators is presented in order to perform calculations of detection theory and the model of the interferometer in chapters 3 and 4 respectively.

Chapter 3 describes modulation techniques and control of the interferometer. The theory of detection is presented, with important cases being calculated.

Chapter 4 derives a full model for the PRM with squeezing, allowing both classical behavior and interaction with quantum noise to be analyzed.

In chapter 5 the experimental setup of the optical configuration and control schemes are described.

Chapter 6 presents results from the first demonstration of quantum noise reduction in a gravitational wave interferometer configuration, and many properties of the interaction with squeezing demonstrated.

Chapter 7 concludes the work and results presented in this thesis.

Chapter 2

Quantum Noise and Squeezing

2.1 Overview

This chapter introduces the theory of quantum noise to be used in modelling in the following chapters. Important states of light used in the experiment are discussed and represented by the 'ball on stick' picture. The method of linearization of operators is used to aid in modelling interferometers in the following chapters. Finally, a brief description of some processes involved in the production of squeezing are presented.

2.2 The Heisenberg uncertainty principle

The limit to the sensitivity of any measurement is imposed by quantum mechanical fluctuations. The Heisenberg uncertainty principle(HUP) describes this limit for a given system. The HUP states that the simultaneous measurement of two non-commuting operators can not have arbitrary precision. If two observables, $\hat{O}^+$ and $\hat{O}^-$ satisfy the commutation relation,

$$[\hat{O}^+, \hat{O}^-] = \xi \tag{2.1}$$

then they satisfy the uncertainty relation,

$$\Delta\hat{O}^+ \Delta\hat{O}^- \geq \frac{|\xi|}{2} \tag{2.2}$$

where $\Delta\hat{O}$ is standard deviation of the operator $\hat{O}$. The standard deviation is defined,

$$\Delta\hat{O} = \sqrt{\langle\hat{O}^2\rangle - \langle\hat{O}\rangle^2} \tag{2.3}$$

and the variance is the square of the standard deviation,

$$V = (\Delta\hat{O})^2 \tag{2.4}$$

The customary example of the uncertainty principle is the position-momentum uncertainty relation. This thesis is concerned with the uncertainty relation for the electromagnetic field. It can be introduced starting with the boson creation and annihilation operators, $\hat{a}^\dagger$ and $\hat{a}$ respectively. They have the commutation relation,

$$[\hat{a}, \hat{a}^\dagger] = 1 \tag{2.5}$$

and the uncertainty relation,

$$\Delta\hat{a}\Delta\hat{a}^\dagger \geq 1/2 \tag{2.6}$$

The creation and annihilation operators are not Hermitian and therefore do not represent observable quantities. The Hermitian operator pair can be defined using these operators,

$$\hat{X}^+ = \hat{a} + \hat{a}^\dagger \tag{2.7}$$
$$\hat{X}^- = i(\hat{a} - \hat{a}^\dagger) \tag{2.8}$$

where $\hat{X}^+$ is the *amplitude quadrature* and $\hat{X}^-$ is the *phase quadrature* of the electromagnetic field.

$$[\hat{X}^+, \hat{X}^-] = 2i \tag{2.9}$$

and associated uncertainty relation is

$$\Delta X^+ \Delta X^- \geq 1 \tag{2.10}$$

This relation shows that simultaneous measurements of phase and amplitude quadratures of the electromagnetic field can not be arbitrarily accurate. In optics experiments, the measurement of fluctuations described here is know as the quantum noise of the light. The *minimum uncertainty state*, i.e. $\Delta\hat{X}^+\Delta\hat{X}^- = 1$, is desirable for the precision measurements in interferometers. The manipulation of the minimum uncertainty state is dealt with in the following section.

2.3 States of light

In this section the light states that are used in the experiment are introduced. To aid the understanding of the light states and how they interact with optical systems a graphical representation is introduced. This is the "ball on stick" picture shown in figure 2.1. In this diagram the length of the stick represents the amplitude of the field and the radius of the ball represents standard deviation of the field. The vertical and the horizontal axes represent the phase and amplitude quadratures, respectively. This picture is analogous to the representation of classical fields on a phaser diagram. Without the ball of noise, the ball on stick picture reduces to the phaser diagram, and the vertical and horizontal axis can be relabelled the imaginary and real parts of electric field.

2.3.1 The coherent state

The *coherent state* of light has a coherent amplitude and minimum uncertainty fluctuations in both quadratures. The standard deviation of the two quadratures is,

$$\Delta X^+ = \Delta X^- = 1 \tag{2.11}$$

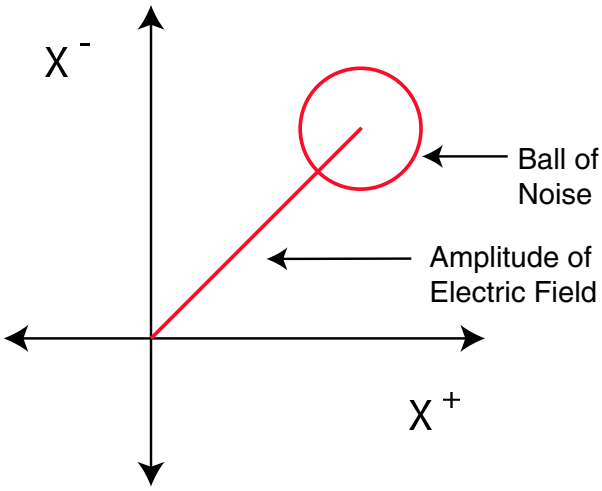

Figure 2.1: Ball on stick picture representation of a state of light. X^- is the phase quadrature and X^+ is the amplitude quadrature.

This noise has a Poissonian distribution [4] and is white, that is, constant across all frequencies. The ball and stick representation of a coherent state is shown in figure 2.2(a). The coherent state is important in experimental optics as the light a laser produces can be well approximated by it [25]. This approximation is valid for a minimum uncertainty state, where there is no technical or classical noise. Light that can be well approximated by a coherent state is known as *shot noise limited* (SNL) light. SNL light is used in most experiments involving high precision optics, such as gravitational wave detection.

2.3.2 The vacuum state

The vacuum state is a special case of the coherent state. It has the same noise statistics, but differs from the coherent state as it has no coherent amplitude. The ball on stick representation of the vacuum state is shown in figure 2.2 (b). The vacuum state also exhibits white noise. As its name suggests, the vacuum state exists in the optical vacuum, which is any region in space where their is not already a light state. It occupies all spatial and polarization modes.

The vacuum state is important in experiments as it couples into optical systems whenever losses of light occur. The losses could be due to a beamsplitter or to absorbtion. In any case, the vacuum state replaces the light that is lost. As more of the light is lost its noise statistics approaches that of the vacuum state. This is an important result which will be referred to throughout this thesis.

2.3.3 The squeezed state

A *squeezed state* of light has the standard deviation of a quadrature less than one. In order to satisfy the HUP, the product with the variance of the other quadrature must be equal or large than one. A amplitude squeezed state has,

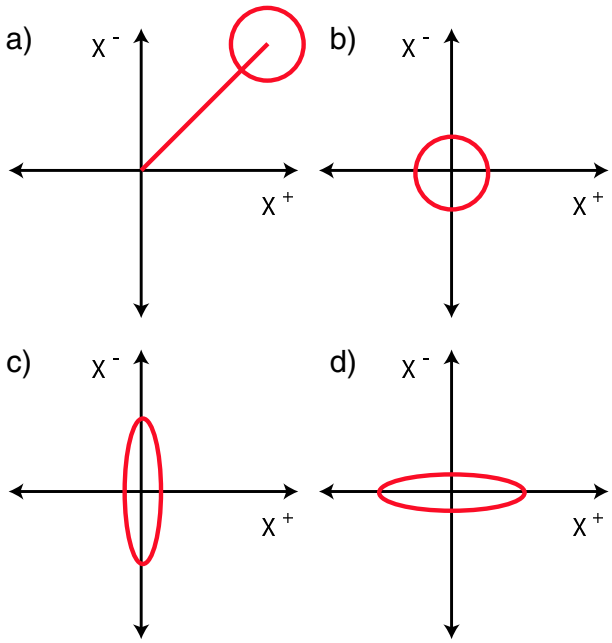

Figure 2.2: Ball and stick picture for four states of light. a) The coherent state. b) The vacuum state. c) and d) represent amplitude and phase squeezed states, respectively.

$$\Delta X^{+} = 1/z \tag{2.12}$$
$$\Delta X^{-} \geq z \tag{2.13}$$

here z is a real number. The larger z is, the larger the degree of squeezing. A amplitude squeezed state with $z = 2$ is shown in figure 2.2 (c). A phase quadrature squeezed state with $z = 2$ is shown in figure 2.2(d). These states are shown with no coherent amplitude. A squeezed state refers only to the noise statistics, it can have any coherent amplitude. A squeezed state with no coherent amplitude is called a *vacuum squeezed state*. A squeezed state with a large coherent amplitude is called a *bright squeezed state*.

The squeezed state can be used to reduce the quantum noise on a measurement in the squeezed quadrature. Without using a squeezed state the accuracy of measurement is limited to the SNL. Of course, if the anti-squeezed quadrature is measured the noise is larger than the SNL.

Current gravitational wave detectors are limited by quantum noise only in the phase quadrature. Therefore, the use of a squeezed state in the phase quadrature could improve to the sensitivity of the measurement to below the SNL. This is the main interest of this thesis.

2.4 Linearization of the operators

When the fluctuations of an electromagnetic field are much smaller than the steady state amplitude, the creation and annihilation operators can be linearized [26]. Each operator is split into two terms, a constant amplitude term and a time varying fluctuations term,

$$\hat{a}(t) \approx \alpha + \delta\hat{a}(t) \tag{2.14}$$
$$\hat{a}^\dagger(t) \approx \alpha^* + \delta\hat{a}^\dagger(t) \tag{2.15}$$

where $\alpha = \langle\hat{a}(t)\rangle$ is the constant amplitude and $\delta\hat{a}(t)$ is the time varying fluctuations of $\hat{a}(t)$. Similarly for the creation operator, $\alpha^* = \langle\hat{a}^\dagger(t)\rangle$ and $\delta\hat{a}^\dagger(t)$ is the time varying fluctuations of $\hat{a}^\dagger$. The fluctuation terms, on average, have no coherent amplitude with magnitude much smaller than α,

$$\langle\delta\hat{a}(t)\rangle = 0 \tag{2.16}$$
$$|\delta\hat{a}(t)| \ll \alpha \tag{2.17}$$

The linearized fluctuation terms of the amplitude and phase quadratures are,

$$\delta X^+(t) = \delta\hat{a}(t) + \delta\hat{a}^\dagger(t) \tag{2.18}$$
$$\delta X^-(t) = i(\delta\hat{a}(t) - \delta\hat{a}^\dagger(t)) \tag{2.19}$$

This representation may be thought of as the mathematical equivalent to the ball on stick picture. Then in figure 2.1,the stick represents α and the ball represents $\delta\hat{a}(t)$. One can also note the comparison with the classical representation of the electric field. Without the time varying fluctuations the state reduces to a classical electric field. As an example of the linearized formalism, the photon number is,

$$n(t) = \hat{a}^\dagger(t)\hat{a}(t) \tag{2.20}$$
$$= (\alpha^* + \delta\hat{a}^\dagger(t))(\alpha + \delta\hat{a}(t)) \tag{2.21}$$
$$= |\alpha|^2 + \alpha^*\delta\hat{a}(t) + \delta\hat{a}^\dagger(t)) + \delta\hat{a}^\dagger(t)\delta\hat{a}(t) \tag{2.22}$$

if we discard second order fluctuation terms and take α to be real we find,

$$n(t) \approx \alpha^2 + \alpha(\delta\hat{a}(t) + \delta\hat{a}^\dagger(t)) \tag{2.23}$$

The expectation value of the photon number is,

$$\langle n(t)\rangle = \alpha^2 \tag{2.24}$$

as the expectation value of the fluctuations is zero. The variance of the photon number is given by,

$$(\Delta n(t))^2 = \langle(n(t))^2\rangle - \langle n(t)\rangle^2 \tag{2.25}$$
$$= \langle(\hat{a}^\dagger(t)\hat{a}(t))^2\rangle - \langle\hat{a}^\dagger(t)\hat{a}(t)\rangle^2 \tag{2.26}$$
$$= \alpha^2\langle(\delta\hat{a}(t) + \delta\hat{a}^\dagger(t))^2\rangle \tag{2.27}$$
$$= \alpha^2\langle(\delta X^+(t))^2\rangle \tag{2.28}$$

where the substitution for the amplitude quadrature fluctuations of the linearized field. As an example for the linearized fluctuation terms, the coherent state has the variance in each quadrature,

$$\langle(\delta X^{+}(t))^{2}\rangle = 1 \tag{2.29}$$
$$\langle(\delta X^{-}(t))^{2}\rangle = 1 \tag{2.30}$$

similarly the vacuum state is described by the same fluctuations.

2.5 The production of squeezed light

This section gives a brief overview of the processes used to generate squeezed light via optical parametric amplification. The generation of squeezed light is not the subject of this research and it should be stated that the device used to generate squeezed light, the *squeezer*, was already built. This was achieved over the period of two Ph.D's by Dr. Ben Buchler and Dr. Ping Koy Lam with details to be found in [22, 27].

The two elements used to produce the squeezed state are two second order nonlinear crystals. The crystal used in this experiment is $MgO : LiNbO_3$, named: magnesium oxide doped lithium niobate.

The squeezing is produced in one crystal, operated as a degenerate optical parametric amplifier(OPA). This relies on a three wave mixing down-conversion process [14]. One of the fields required, the pump, is at twice the frequency of the signal and the idler. This is produced in the second crystal by a up-conversion process called second harmonic generation(SHG).

An illustration of the two processes is shown in figure 2.3.

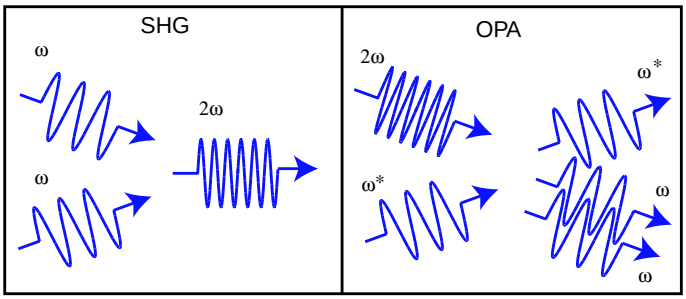

Figure 2.3: Second harmonic generation(SHG) is a four wave mixing process where two photons of frequency ω combine into one photon of twice the frequency 2ω. The degenerate optical parametric amplifier(OPA) process has one photon at frequency 2ω split into two at frequency ω.

2.5.1 Second harmonic generation

Second harmonic generation, or frequency doubling is a degenerate case of three wave mixing process. In the nonlinear medium two photons of frequency, ω_1 combine to form one photon at twice the frequency,

$$\omega_2 = 2\omega_1 \tag{2.31}$$

This condition is required by conservation of energy. In our experiment the Nd:YAG laser light@1064 nm is converted to pump@532 nm. Conservation of momentum requires the *phase matching* condition [14],

$$\mathbf{k}_2 = 2\mathbf{k}_1 \tag{2.32}$$

where $\mathbf{k}$ is the wavevector of the photon. If the photons are co-propagating this simplifies to

$$\frac{n_2\omega_2}{c} = 2\frac{n_1\omega_1}{c} \tag{2.33}$$

where n_2, n_1 are the refractive indices for the two frequencies ω_2, ω_1 respectively and c is the speed of light in vacuum. This equation shows that the phase matching condition requires that the refractive indices to be the equal at both frequencies,

$$n_2 = n_1 \tag{2.34}$$

If this condition is not satisfied (which is the case for most materials) SHG does not occur. The technique used to phase match in $MgO : LiNbO_3$ is known as *type I phase matching*. This crystal has different refractive indexes for the orthogonal polarizations. Using this property the refractive index for the two frequencies can be set to be equal by choosing the correct orientation for each polarization. This is done for particular temperature, as the refractive index of the medium is highly sensitive to temperature. Keeping the temperature controlled is required. Basic control and experimental details required to operate the squeezer are introduced in chapter 5.

2.5.2 Squeezing from a optical parametric amplifier

The squeezed light is produced in the OPA via parametric down-conversion. The pump photon, provided by the SHG, is split into two photons, referred to as the signal and the idler. In our case the signal and idler photons are frequency degenerate. As the pump is produced in the SHG with input from the same laser as the signal the pump is exactly twice the frequency of the signal. The idler and signal that leak out of the OPA is squeezed light. Parametric down conversion is phase dependent process and as such when viewed on a ball on stick diagram, in the figure 2.4, the effect looks as if there is a stretching force on the X^+ axis and compressing force on the X^- axis. The process requires phase matching, which again achieved through temperature control of the crystal. The figure also shows that the phase of the pump relative to the signal determines if amplification or de-amplification occurs. The noise on the coherent amplitude also follow this. In the experiment we use the de-amplified amplitude squeezed beam.

2.6 Summary

This chapter has introduced quantum noise with the HUP and described squeezing and other important states of light used in the experiment. The method of linearization of the operators has been presented to simplify modelling in the following chapters. Finally we have briefly looked at the nonlinear elements involved in squeezing production.

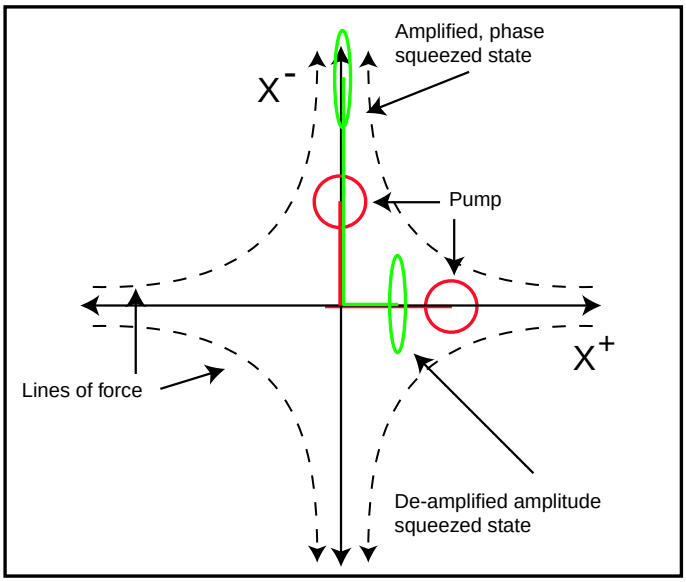

Figure 2.4: The phase dependence of the optical parametric amplification process can be represented by the existence of lines of force towards the phase quadrature.

Chapter 3

Interferometer Control and Detection Theory

3.1 Overview

This chapter introduces techniques used to control the interferometer and some background to understand these. The second half of the chapter introduces the detection of light with emphasis on methods to detect small amplitude signals.

3.2 Introduction to control

The control of the interferometer is extremely important in a gravitational wave detector. Each degree of freedom of the interferometer requires monitoring and control to hold lengths to sub-nanometer accuracy. The control of each degree of freedom requires three elements;

- the monitoring of the current operating condition,
- the comparison of the current to the desired operating conditions,
- feedback to cancel the difference.

The PRM with squeezing requires the control of three length degrees of freedom. The squeezer has an additional four length degrees of freedom. Each degree of freedom has to be *locked* on the desired operating point simultaneously, for the experiment to be operational. The different techniques used to lock each degree of freedom rely on the production of an *error signal*. The error signal has an anti-symmetric form and is proportional to the difference of the current and desired operating conditions. The error signal is fed back to the system, with the appropriate electronic filtering and gain, to correct for discrepancy between the current and desired operating conditions.

3.3 Phase and amplitude modulation

Phase modulation(PM) and amplitude modulation(AM) on an optical field can be used to readout of the status of a optical system and obtain an error signal. PM or AM can be imparted on a optical field using an electro-optic modulator(EOM). An EOM consists of a crystal that exhibits the Pockels effect [14] with a time varying voltage applied across it. The Pockels effect is the change of refractive index with applied voltage. Usually, the applied voltage is at a single frequency, which modulates the effective crystal length

at that frequency. This modulates the phase of light transmitted through the crystal. Sinusoidal PM of a carrier field, α, is mathematically represented by,

$$\alpha = \alpha_0 \mathrm{e}^{i(\omega_c t + A \sin \omega_m t)} \tag{3.1}$$

here α_0 is a constant amplitude[1] and ω_c is the carrier angular frequency. The modulation is at angular frequency, ω_m and has modulation depth, A. The modulation depth corresponds to the amount of light coupled from the carrier into the sidebands(usually on order of 5%). For small A, the above equation can be approximated by the first term in a Taylor expansion.

$$\begin{aligned} \alpha &\approx \alpha_0 \mathrm{e}^{i\omega_c t}(1 + iA \sin \omega_m t) && (3.2) \\ &\approx \alpha_0 \mathrm{e}^{i\omega_c t}(1 + \frac{A}{2}\mathrm{e}^{i\omega_m t} - \frac{A}{2}\mathrm{e}^{-i\omega_m t}) && (3.3) \end{aligned}$$

This shows three terms; a carrier field and sidebands at $\pm$ the modulation frequency. The carrier and sinusoidal PM sidebands are represented in figure 3.1 a). The axes are frequency in the horizontal direction and imaginary and real parts of the electric field in the vertical and coming out of the page respectively. This figure also shows cosine PM, sine AM and cosine AM.

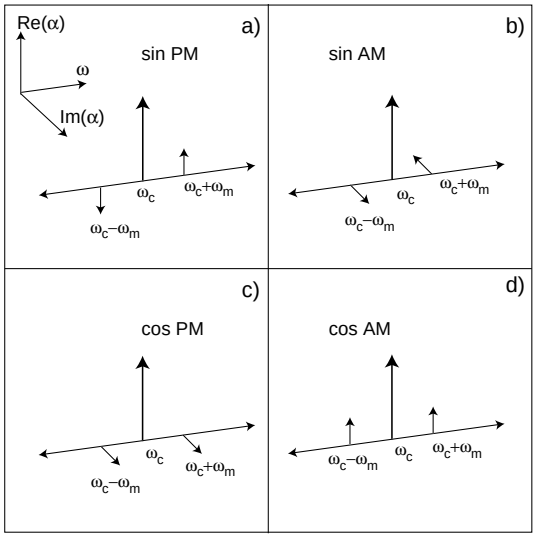

Figure 3.1: sinusoidal AM, PM and cosine AM and PM.

The detection of AM and PM on a optical field is important. PM can not be directly detected on a photodetector as only the phase of the field is changing. AM can be directly detected, as the total intensity of an AM field is changing. This differentiation between PM and AM becomes is used in the generation of an error signal.

[1]The quantum fluctuations are neglected in this calculation as they are small compared with the amplitude of PM.

3.4 The Fabry-Perot cavity

The optical cavities described in this thesis are a slight variation of the Fabry-Perot cavity. Some of the important parameters of the cavity include; the free spectral range, FSR; the finesse, $\mathcal{F}$; and the linewidth, l.

$$FSR = \frac{c}{2L} \tag{3.4}$$

$$\mathcal{F} = \frac{\pi(R_1 R_2)^{1/4}}{1-\sqrt{R_1 R_2}} \tag{3.5}$$

$$l = \frac{FSR}{F} \tag{3.6}$$

here c is the speed of light and L is the length of the cavity. The power reflectivity[2] of the two mirrors of the cavity are R_1 and R_2. The FSR gives a measure of the frequency separation between adjacent longitudinal modes. The finesse is analogous to the quality or Q of a electronic circuit. The linewidth is the full-width-half maximum of the cavity resonance.

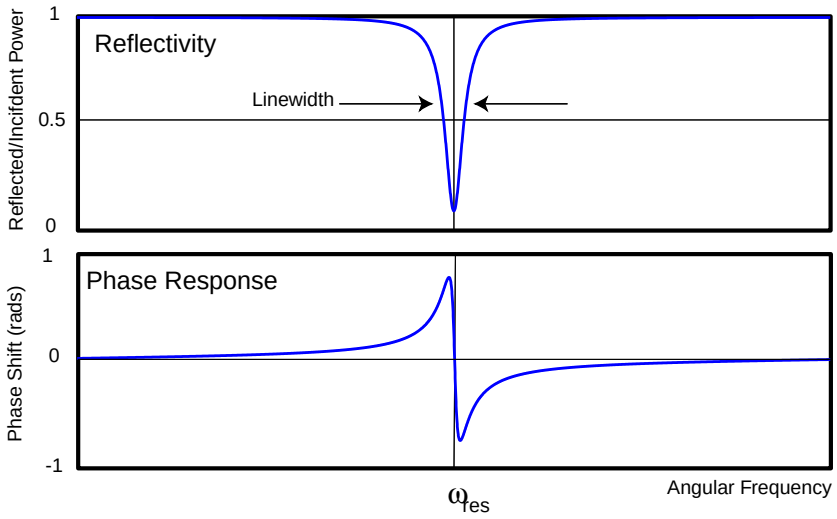

Figure 3.2: The magnitude and phase response of a field undergoing reflection from an undercoupled Fabry-Perot cavity . ω_{res} is the angular resonant frequency

The phase response on reflection and reflectivity for a undercoupled Fabry Perot cavity [14] are shown in figure 3.2. The phase response inside the cavity linewidth has an antisymmetric form which crosses zero on resonance. Well outside the cavity linewidth the reflected field receives almost no phase shift. The reflectivity on resonance is low, as the field is mostly transmitted. Off resonance the reflectivity is larger and approaches 1 outside the linewidth.

The complex reflectivity of a cavity is important for the locking techniques presented in the following sections, but also for the squeezed light interaction with the PRM as

[2]The amplitude reflectivity $r = \sqrt{R} = \sqrt{1-t^2-a^2}$

discussed in chapter 4.

3.5 Interaction of PM with an optical cavity

The PM sidebands on a carrier can be used as a reference for the interaction with a cavity. This can be understood by use of an example. Consider the field described by equation 3.3 incident on the cavity with properties shown in figure 3.2. Assume the modulation frequency much larger than the cavity linewidth. The reflected field is measured on a photodetector as the carrier frequency is varied. When the carrier field is on resonance

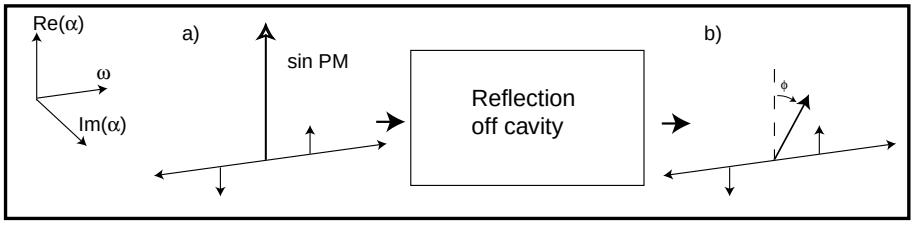

Figure 3.3: a) The phase modulated carrier field is incident on the cavity slightly off resonance. b) The reflected field consists of an attenuated and phase shifted carrier and the phase modulation sidebands which, because they are well outside the linewidth of the cavity, do not receive any phase shift or not attenuation on reflection.

a small fraction of the incident light at ω_c is reflected and it receives no phase shift. The sidebands, at ω_m, are well outside the linewidth of the cavity. They are completely reflected and receive no phase shift. If the carrier frequency is lowered slightly, still within the cavity linewidth, the reflected field at ω_c increases and receives a positive phase shift, ϕ. The sidebands, still well outside the cavity linewidth, remain unchanged. This case is shown in figure 3.3. Instead, if the carrier frequency is higher than the resonance frequency, still within the cavity linewidth, the reflected field increases and this time receives a negative phase shift, $-\phi$. Again the sidebands are reflected unchanged.

Since the interaction of the carrier and PM sidebands with the cavity is different, with some novel thinking an error signal can be extracted.

3.6 Locking Techniques

The two locking techniques used to lock the degrees of freedom are discussed in this section.

3.6.1 Pound Drever Hall locking

Pound-Drever-Hall (PDH) locking [28] is a commonly used technique in optics to measure and control a cavity on resonance. PDH is used in the experiment to lock the power recycling cavity. This is the standard technique in long baseline interferometers. We also use PDH to locked the relative phase of the squeezed light to the interferometer, and in the squeezer for 3 additional locking loops.

The PDH error signal is obtained by the measurement of the relative phase of the carrier field and PM sidebands reflected off the cavity. The previous section showed

that when near resonance, the reflected field at ω_c receives a phase shift, ϕ whilst the sidebands at ω_m are unchanged. This is shown in figure 3.3. Equivalently, this can be drawn with the carrier having no phase shift and the sidebands with the phase shift $-\phi$. This is shown in the figures 3.4 a) for the case where the carrier receives a positive phase shift and b) where the carrier receives a negative phase shift. These fields can be decomposed into a sum of the original sin PM and a component of sin AM. In figure 3.4 a) the positive phase shift means the sin AM component has a positive value. In figure 3.4 b) the sin AM component is negative. On resonance the carrier receives no phase shift, therefore there is no sin AM component. The sin AM component gives a antisymmetric signal used as the error signal for PDH locking.

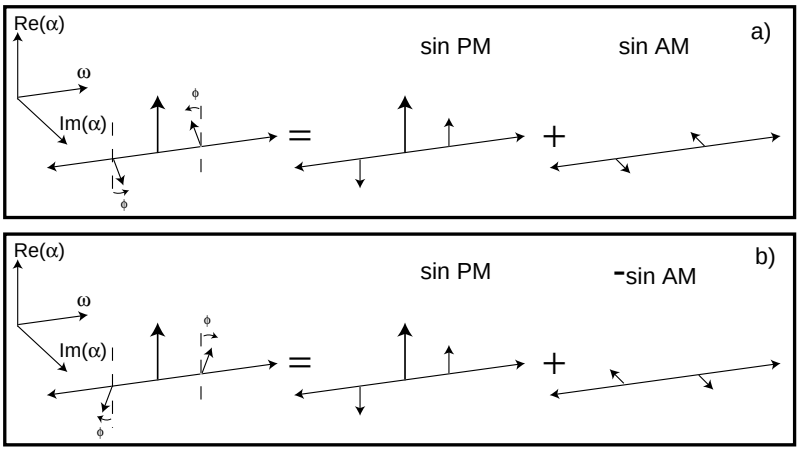

Figure 3.4: The reflected fields can be redrawn equivalently with the carrier pointing straight up and the sidebands having the phase shift. This picture can be decomposed into a sum of the original sin PM and a component of sin AM. If the carrier frequency is slightly lower in frequency the carrier

The experimental layout for a PDH locking system is shown in figure 3.5. The incoming light is phase modulated with a frequency well outside the linewidth of the cavity. The reflected light is measured on the photodetector. The detected signal (the amount of sin AM) at the modulation frequency is demodulated electronically. Demodulation transfers the measured signal at ω_m down to DC to be fed back as an error signal. It also introduces a term at $2\omega_m$ which is removed by a low pass filter. The error signal is used lock the cavity length on resonance with the laser frequency using the PZT. It can also be used to lock the laser frequency to the cavity resonance.

3.6.2 Offset locking

Offset locking [19] is a simple technique used to lock an interferometer slightly off resonance. We use it to lock the differential mode of the Michelson interferometer. A topical technique, it has been proposed for use in the Advanced LIGO configuration, as it presents many benefits over modulation techniques.

The error signal is derived by subtracting a DC offset from the power transmitted to the output of the Michelson. The figure 3.6 shows the power at the output as a function of the phase difference between the fields in the arms, $\Delta\Phi$. It also shows the power at the

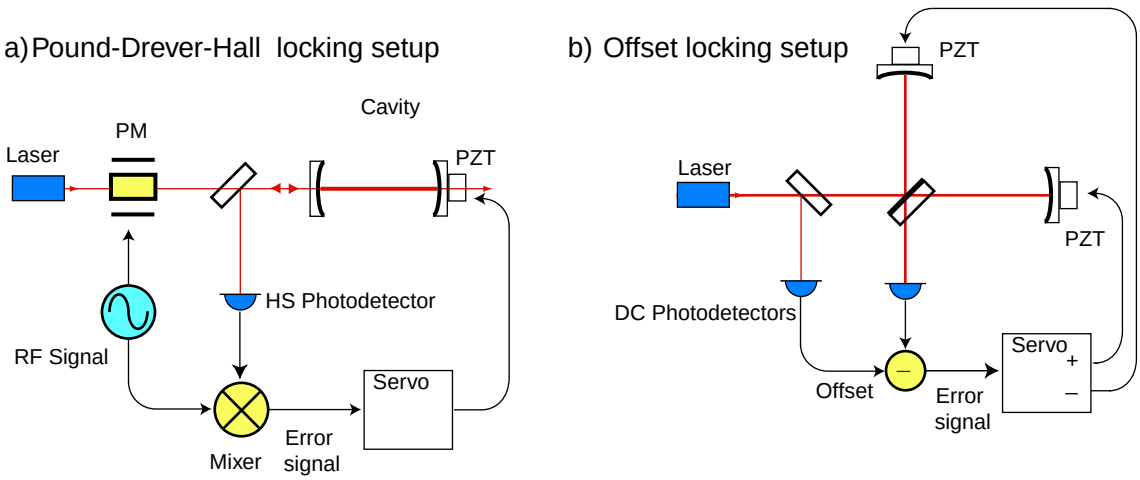

Figure 3.5: Locking techniques experimental setup; a) Pound-Drever-Hall locking. PM-Phase modulation, RF Signal- Radio frequency signal. PZT-Peizo electric transducer, HS Photodetector-High speed photodetector. The phase modulation sidebands are imparted on to the carrier field before incidence with the cavity. The reflected field is detected on a high speed photodetector before being mixed down, producing an error signal. The error signal is processed by a servo then fed to one cavity mirror PZT to control the length of the cavity, controlling the cavity resonance to the laser frequency. b) The Offset locking setup has a tap off before the Michelson interferometer to obtain a DC offset. This is subtracted from the DC power at the dark port, producing the error signal. This is fed into the servo which filters and outputs two opposite polarities error signals, fed to different mirrors to control the relative arm length.

output with a DC offset subtracted. This is the error signal to lock the Michelson differential mode. The operating point is slightly offset from the usual dark fringe. This point can be tuned by changing the DC offset. We obtain the DC offset optically, by tapping off some light before the Michelson. This measure is taken rather than simply using a voltage supply so that the offset lock point is isolated from the laser power fluctuations. For example, if the laser power increases, the power in the Michelson and the offset voltage increase by the same proportion, leaving the lock point unchanged. The setup is shown in figure 3.5 (b). The error signal is fed back differentially to the Michelson arms.

All current long base-line detectors use a RF modulation scheme similar to that of PDH locking also called *Frontal* or *Schnupp modulation* [29]. Offset locking requires no modulation, so unlike Schnupp/frontal modulation, the signal readout does not require demodulation. This is a benefit as the squeezing is only required at the GW signal frequencies. If modulation techniques are used, squeezing is also required at the signal frequency and twice the modulation frequency $\pm$ the signal frequency [7]. This simplification on the requirements for the squeezed light in a GW detector is valuable.

In high power systems, such as the LIGO interferometers, phase modulator crystals heat up, introducing undesirable effects such as wavefront distortion. Offset locking does not encounter this problem. The other advantage of offset locking is that it does not require the Michelson to have a Macroscopic arm length mismatch (as is the case for Schnupp modulation). This is an advantage for the bench top squeezing system as a macroscopic arm length mismatch would introduce extra losses for the squeezing at high frequencies.

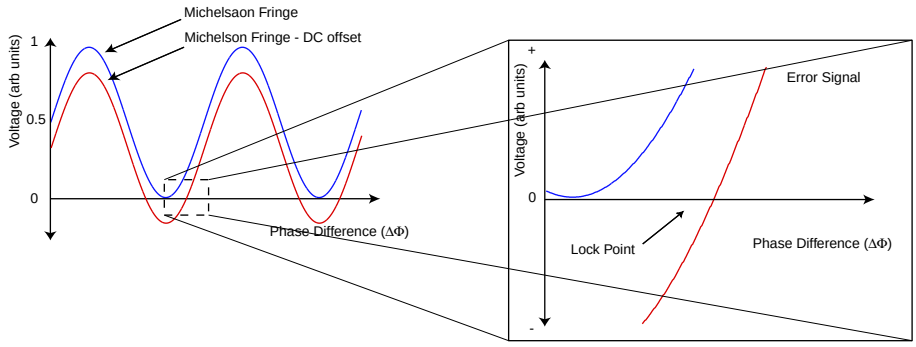

Figure 3.6: The offset locking error signal is obtained by taking a DC offset from the voltage at the detector at the output of the interferometer.

3.7 Detection theory

This section introduces the theory of the detection. The techniques used are direct detection and standard homodyne detection. This is done using the method of linearized operators. These are discussed in terms of measurements and of a GW signal. Finally, the effect of inefficient detection is reviewed.

3.7.1 Direct detection

The direct detection of light is performed on incidence with a photodiode. The current out of the photodiode, the *photocurrent*, is proportional to the incident intensity or photon number. The photocurrent is converted to a voltage and viewed on a CRO for a DC value or a spectrum analyzer for broadband detection. For a light field, $\hat{a}$, the photon number using linearized operators, derived in equation 2.23 is given by,

$$n(t) \approx |\alpha|^2 + \alpha\delta X_a^+(t) \tag{3.7}$$

then the photocurrent is,

$$\begin{aligned} i(t) &\propto n(t) \\ &\propto |\alpha|^2 + \alpha\delta X_a^+(t) \end{aligned} \tag{3.8}$$

This can also be represented in the frequency domain. Taking the Fourier transform of the linearized operators, $\hat{a}(\omega) = \alpha\delta(0) + \delta\hat{a}(\omega)$, then calculating the photon number once more,

$$n(\omega) \approx |\alpha|^2\delta(0) + \alpha\delta X_a^+(\omega) \tag{3.9}$$

to give the photocurrent,

$$\begin{aligned} i(\omega) &\propto n(\omega) \\ &\propto |\alpha|^2\delta(0) + \alpha\delta X_a^+(\omega) \end{aligned} \tag{3.10}$$

This equation shows the photocurrent contains a large DC term plus the frequency dependent amplitude quadrature fluctuations, scaled by the amplitude of the field. It is interesting to note the absence of phase quadrature fluctuations in this equation. When detecting a large amplitude field, only the fluctuation in quadrature with the field amplitude become important. This is the principle used for the *local oscillator* explored in the following section.

3.7.2 Standard Homodyne

The sensitivity of measurement of small optical signal, $\hat{a}$ can be improved by beating with a large amplitude local oscillator(LO), $\hat{b}$, using the *standard homodyne configuration*. This configuration is shown in the figure 3.7. The fields $\hat{a}$ and $\hat{b}$ are combined on a beamsplitter, with each output detected with a photodetector. The sum and difference of the photocurrents is taken. The fields at the respective output ports, $\hat{c}$ and $\hat{d}$ can be calculated. The phase difference between the fields at interference is θ. For a balanced beamsplitter we find[3],

$$\hat{c} = \frac{1}{\sqrt{2}}[\hat{a} + i\hat{b}\mathrm{e}^{i\theta}] \tag{3.11}$$

$$\hat{d} = \frac{1}{\sqrt{2}}[i\hat{a} + \hat{b}\mathrm{e}^{i\theta}] \tag{3.12}$$

The phase difference between the fields in this calculation is arbitrary. For mathematical convenience the a $-i$ phase shift to $\hat{b}$ is introduced giving,

$$\hat{c} = \frac{1}{\sqrt{2}}[\hat{a} + \hat{b}\mathrm{e}^{i\theta}] \tag{3.13}$$

$$\hat{d} = \frac{1}{\sqrt{2}}[\hat{a} - \hat{b}\mathrm{e}^{i\theta}] \tag{3.14}$$

using linearized formalism,

$$\hat{c} = \frac{1}{\sqrt{2}}[\alpha + \delta\hat{a} + (\beta + \delta\hat{b})\mathrm{e}^{i\theta}] \tag{3.15}$$

$$\hat{d} = \frac{1}{\sqrt{2}}[\alpha + \delta\hat{a} - (\beta + \delta\hat{b})\mathrm{e}^{i\theta}] \tag{3.16}$$

[3]The notation used to calculate fields: Introduce an i on transmission of the beamsplitter. For a balanced(50:50) beamsplitter each transmission and reflection receives a factor of $1/\sqrt{2}$

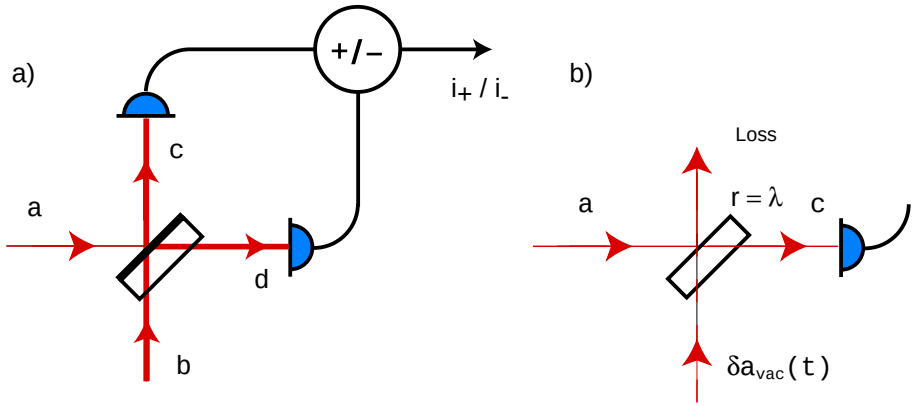

Figure 3.7: a) The standard homodyne configuration. The small signal $\hat{a}$ is interfered on a balanced beamsplitter with the local oscillator, $\hat{b}$. The detected photocurrents can be either added or subtracted. b) A model for inefficient detection. A mirror with reflectivity equal to the loss of detection is placed in front of an ideal photodetector.

Taking the photon number at each detector, discarding the 2nd order fluctuation terms,

$$\begin{aligned}\hat{c}^\dagger\hat{c} &\approx \frac{1}{2}[|\alpha|^2+|\beta|^2+2\alpha\beta\cos\theta+ \\ &\quad \alpha(\delta X_a^+ + \delta\hat{b}^\dagger e^{-i\theta}+\delta\hat{b}e^{i\theta})+ \\ &\quad \beta(\delta X_b^+ + \delta a^\dagger e^{i\theta}+\delta\hat{a}e^{-i\theta})] \qquad (3.17)\\ \hat{d}^\dagger\hat{d} &\approx \frac{1}{2}[|\alpha|^2+|\beta|^2-2\alpha\beta\cos\theta+ \\ &\quad \alpha(\delta X_a^+ - \delta\hat{b}^\dagger e^{-i\theta}-\delta\hat{b}e^{i\theta})+ \\ &\quad \beta(\delta X_b^+ - \delta\hat{a}^\dagger e^{i\theta}-\delta\hat{a}e^{-i\theta})] \qquad (3.18)\end{aligned}$$

here the substitutions for δX_a^+ and δX_b^+ have been made. If $|\alpha| \ll |\beta|$ terms without the amplitude of the LO, β, are discarded. We are left with,

$$c^\dagger c \approx \frac{1}{2}[|\beta|^2+2\alpha\beta\cos\theta+\beta(\delta X_b^+ + \delta X_a^+\cos\theta+\delta X_a^-\sin\theta)] \qquad (3.19)$$

$$d^\dagger d \approx \frac{1}{2}[|\beta|^2-2\alpha\beta\cos\theta+\beta(\delta X_b^+ - \delta X_a^+\cos\theta-\delta X_a^-\sin\theta)] \qquad (3.20)$$

for the fields at the two photodetectors. Here the fluctuation terms have been simplified using Eulers equation and the substitutions for δX_a^- and δX_b^-.

These equations are not particularly enlightening. The largest term is the LO beating with itself, $|\beta|^2$. There are many cross terms that involve fluctuations which have phases difference dependence. Taking the sum and difference photocurrents we find more insight.

$$i_+ \propto |\beta|^2 + \beta\delta X_b^+ \tag{3.21}$$
$$i_- \propto 2\alpha\beta\cos\theta + \beta[\delta X_a^+ \cos\theta + \delta X_a^- \sin\theta] \tag{3.22}$$

The sum of photocurrents gives the same fields as if the LO was directly detected. This is because of its large coherent amplitude and our assumption of the signal being negligible. Taking the difference, we find many terms are cancelled out, leaving a cross term between the amplitudes of the LO and signal, with dependence on the phase between them. To measure the amplitude of the signal it is ideal to have the $\theta = 0$, that is, in quadrature with the LO. We also find two terms involving the amplitude and phase quadratures fluctuations of the signal with phase dependence. By tuning the phase difference, θ, measurement of either phase or amplitude quadrature fluctuations of the signal can be performed. It is important to note the noise of the LO does not enter into this equation. This however, is only the case for perfect subtraction and 50:50 beamsplitter.

This calculation indicates, if one wants to measure a small amplitude signal α, it would it desirable to have the minimum fluctuations on α and the phase difference with the LO, $\theta = 0$. If the signal has squeezed fluctuations in the correct quadrature the measured noise can be reduced.

3.7.3 The measurement of squeezing

The measurement of squeezing before it interacts with the interferometer in the experiment is performed using the standard homodyne. In this case, the small amplitude signal, $\hat{a}$ is the squeezing and the LO, $\hat{b}$ is a large amplitude coherent state. The difference current is taken, and the phase difference, θ is scanned. The fluctuations in each quadrature can be easily measured. A shot noise limit can be easily obtained by blocking the squeezed field and taking the difference photocurrent. In this case the small signal is the vacuum state $\hat{a} = \delta\hat{a}_{vac}$

3.7.4 The Local oscillator in gravitational wave detectors

A gravitational wave detector uses a LO to improve the measurement sensitivity of the GW signal. The LO for the signal is the field also used for the control of the differential mode of the Michelson. In our interferometer, since we use offset locking, the LO is the DC field coupled to the output of the interferometer when the arms are offset. A vector diagram of fields in the Michelson arms and the resultant, the LO, is shown in figure 3.8. The GW signal, which arises dues to differential motion of the arms, is in phase with the LO. The coherent state fluctuations are shown on the signal. This figure shows that only the noise in phase with the signal is important. This is exploited, by the use of squeezing. A full model of this is found in the following chapter.

3.8 Inefficient measurements

The efficiency of a shot noise or sub-shot noise experiment is important. Inefficiency couples in vacuum fluctuations, which degrade the signal. Any linear inefficiency, or loss, before detection can be represented by a simple model is shown in figure 6.2. A

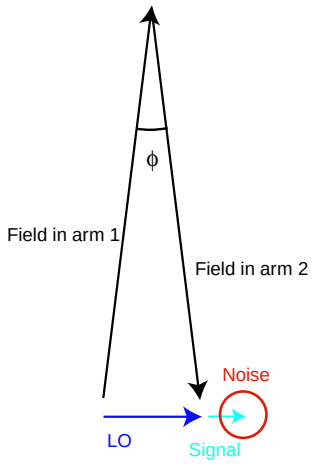

Figure 3.8: A vector diagram of the fields in the Michelson arms and the resultant, the local oscillator. A GW signal is in phase with the local oscillator.

mirror with power reflectivity equal to the loss, λ, is placed before an ideal photodetector. The efficiency is defined,

$$\eta = 1 - \lambda \tag{3.23}$$

The field at $\hat{c}$ is a sum of the field $\hat{a}$ and the vacuum scaled appropriately,

$$\hat{c} = \sqrt{\eta}\hat{a} + \sqrt{1-\eta}\delta v \tag{3.24}$$

in the linearized formalism,

$$\hat{c} = \sqrt{\eta}(\alpha + \delta\hat{a}) + \sqrt{1-\eta}\delta v \tag{3.25}$$

Taking the photon number for the field at the detector,

$$\begin{aligned} \hat{c}^\dagger\hat{c} &= (\sqrt{\eta}(\alpha + \delta\hat{a}^\dagger) + \sqrt{1-\eta}\delta v^\dagger)(\sqrt{\eta}(\alpha + \delta\hat{a}) + \sqrt{1-\eta}\delta v) && (3.26)\\ &\approx \eta(|\alpha|^2 + \alpha\delta X_a^+) + \sqrt{\eta(1-\eta)}\alpha\delta X_v^+ && (3.27)\end{aligned}$$

The loss means that the signal is smaller (first term) but also the vacuum fluctuations are added (second term). It can be seen that if the fluctuations on the field $\hat{a}$ are squeezed, the loss degrades this.

3.8.1 Mode mismatch in homodyne

Mode mismatch describes the case when two fields don't interfere completely. This can arise due to different effects, the outcome is the same as a linear loss. Mode mismatch occurs when two fields have; different spatial distribution, different wavefront curvatures or different polarizations. This is modelled the same way photodetector loss is as

in 6.2 b). A measure of the interference or mode matching is given by the fringe visibility. When two fields of the same coherent amplitude are combined on a balanced beamsplitter and the phase between them scanned the fringe visibility is defined by looking at the minimum and maximum voltages on one photodetector,

$$F_{vis} = \frac{V_{max} - V_{min}}{V_{max} + V_{min}} \tag{3.28}$$

The interference efficiency is defined as the square of the fringe visibility.

$$\eta = F_{vis}^2 \tag{3.29}$$

3.8.2 Electronic noise

The photodetector and signal processing units introduce uncorrelated electronic noise to any measurement. This noise can be made to be negligible and reduced to much below shot noise by having high enough power on the detectors.

3.9 Chapter summary

In this chapter we have introduced some background to modulation theory and the complex reflectivity of a Fabry-Perot cavity. This is used in the discussion of the techniques used to control the interferometer. Finally we have calculated some detection theory and discussed how this relates to gravitational wave detection.

Chapter 4

Theory of a Power Recycled Michelson Interferometer with Squeezed Light

4.1 Overview

This chapter introduces a theoretical model of a power recycled Michelson (PRM) with squeezed light using linearized operators. The interaction of squeezing, vacuum fluctuations and losses with the interferometer is examined. The model is used to analyze both the classical behavior of the interferometer and the quantum fluctuations at the output.

4.2 Equivalent optical circuits

Interferometer configurations used for gravitational wave detection are becoming increasingly complex. To understand the behavior and operation of these systems it is useful to use an equivalent optical circuit. This mathematically represents the transfer function of the interferometer. A complex configuration can be simplified by breaking it into sub-configurations and representing each with a transfer function. Then combining the transfer functions the full configuration transfer function is obtained. This technique results in the most complex interferometer being represented by a single transfer function. It is analogous to Thevenin or Norton circuits in electronics, where a transfer function is used to represent complex electrical circuits.

The components in the interferometer have linear media[1] and the transfer functions are derived in steady state. These conditions make equivalent transfer functions very powerful.

4.2.1 The Michelson interferometer

The transfer functions for the reflectivity and transmission of the Michelson interferometer are found by dividing equations 1.2, 1.3 by the incident field,

[1] The model of the squeezer is not derived here. As the squeezer contains cavities with non linear crystals, these conditions would not be valid

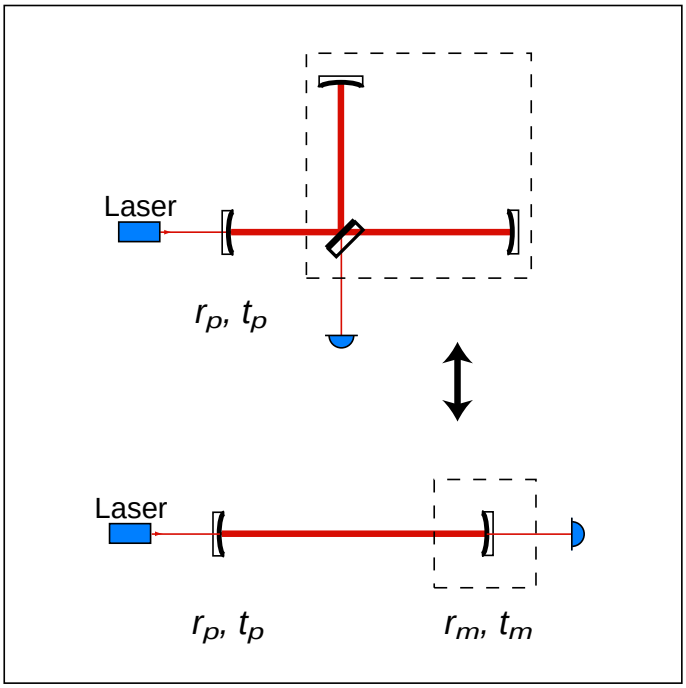

Figure 4.1: A power recycled Michelson can be represented by a Fabry Perot cavity, with the back mirror having reflectivity r_m, and transmissivity t_m equal to that of a Michelson. The power mirror reflectivity is r_p and transmissivity t_p

$$r_m = \frac{\alpha_{ref}}{\alpha_{in}} = \cos 2\phi_d e^{i2\phi_m} \tag{4.1}$$

$$t_m = \frac{\alpha_{trans}}{\alpha_{in}} = \sin 2\phi_d e^{i2\phi_m} \tag{4.2}$$

where $\phi_d = \omega_c \Delta L/c$ and $\phi_m = \omega_c L/c$ represent the differential and common phase shifts the light recieves in the Michelson arms, respectively.

Using these transfer functions a Michelson interferometer can be replaced with a mirror with t_m and r_m. Then the PRM reduces to a Fabry Perot cavity as shown in figure 4.1. The Michelson mirror has variable reflectivity and transmission, however, whilst operational it is locked to a constant value.

4.3 Power recycled Michelson with Squeezing

In this section a mathematical model of the PRM with squeezing is derived using the linearized formalism. The model describes the fields and respective transfer functions to the output. It is used to analyze the behavior of the interferometer and specifically, the quantum noise at the output.

A schematic of the experimental setup for the PRM with squeezing is shown in figure

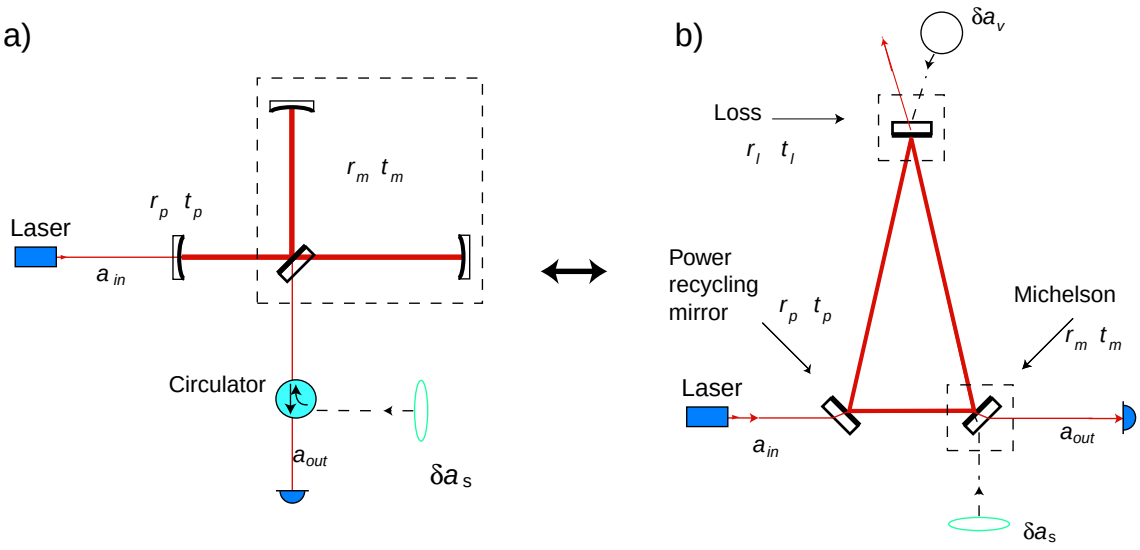

Figure 4.2: The model of the power recycled Michelson interferometer with squeezing injected into the dark port is simplified to a ring cavity. The three mirrors represent different elements of the power recycled Michelson interferometer. The top mirror is used to represent loss in the cavity, here vacuum fluctuations enter. The first mirror is the power recycling mirror. The final mirror represents the Michelson interferometer. The squeezing reflects off the last mirror

4.2 (a). A equivalent model is shown in figure 4.2 (b). This representation uses a Fabry Perot ring cavity. The three mirrors represent: The power recycling mirror with reflectivity and transmisson, r_p,t_p, the Michelson interferometer with r_m,t_m and losses in the cavity with, r_l,t_l. The loss mirror transmission, t_l is equal to the total round trip loss in the cavity.

4.3.1 Fields in the interferometer

The fields in the model are represented in the frequency domain using the linearized operators. The three fields that couple to the output of the interferometer are; the carrier, the squeezing and the vacuum fluctuations,

$$\hat{a}_{in}(\omega) = \alpha + \delta\hat{a}_{in}(\omega) \tag{4.3}$$
$$\hat{a}_s(\omega) = \delta\hat{a}_s(\omega) \tag{4.4}$$
$$\hat{a}_v(\omega) = \delta\hat{a}_v(\omega) \tag{4.5}$$

The carrier field is represented by the coherent state[2]. It has the DC amplitude, $\alpha = \alpha\delta(0)$ and fluctuations, $\delta\hat{a}_{in}(\omega)$. The squeezed field is represented by the fluctuating term, $\delta\hat{a}_s(\omega)$. It has small coherent amplitude, $s \ll \alpha$ not included in this model. The vacuum state is $\delta\hat{a}_v(\omega)$.

[2]This representation is valid for the operational frequency range, since it it shot noise limited

4.3.2 The transfer functions of the interferometer

Each of the fields has a different transfer function since it enters the cavity from a different port. The laser field is incident on the power mirror. The squeezing field is incident on the Michelson interferometer beamsplitter, or in the simplified picture, the last mirror of the Fabry Perot ring cavity. The vacuum fluctuations enter the mirror which represents the losses in the cavity.

The transfer functions for the respective fields in the frequency domain are,

$$T_{\alpha}(0) \quad \leftrightarrow \quad \alpha \tag{4.6}$$
$$T_{\delta a_{in}}(\omega) \quad \leftrightarrow \quad \delta\hat{a}_{in}(\omega) \tag{4.7}$$
$$T_{\delta a_{s}}(\omega) \quad \leftrightarrow \quad \delta\hat{a}_{s}(\omega) \tag{4.8}$$
$$T_{\delta a_{v}}(\omega) \quad \leftrightarrow \quad \delta\hat{a}_{v}(\omega) \tag{4.9}$$

Using these transfer functions, the annihilation and creations operators at the output can be defined,

$$\hat{a}_{out}(\omega) = T_{\alpha}(0)\alpha + T_{\delta a_{in}}(\omega)\delta\hat{a}_{in}(\omega) + T_{\delta a_{s}}(\omega)\delta\hat{a}_{s}(\omega) + T_{\delta a_{v}}(\omega)\delta\hat{a}_{v}(\omega) \tag{4.10}$$
$$\hat{a}^{\dagger}_{out}(\omega) = T_{\alpha}(0)\alpha + T_{\delta a_{in}}(\omega)\delta\hat{a}^{\dagger}_{in}(\omega) + T_{\delta a_{s}}(\omega)\delta\hat{a}^{\dagger}_{s}(\omega) + T_{\delta a_{v}}(\omega)\delta\hat{a}^{\dagger}_{v}(\omega) \tag{4.11}$$

here each field is multiplied by the respective transfer function. The transfer functions are similar to that of a simple Fabry Perot ring cavity. The transfer function for the carrier DC component is[3],

$$T_{\alpha}(0) = -\frac{t_p t_m \mathrm{e}^{i\phi_c}}{1 - r_p r_m r_l \mathrm{e}^{i2\phi_c}} \tag{4.12}$$

where ϕ_c is the cavity round trip phase shift for the carrier. When the experiment is operational the carrier is kept on resonance with the cavity, thus $\phi_c = n2\pi$ where n is an integer. On resonance the transfer function becomes,

$$T_{\alpha}(0) = -\frac{t_p t_m}{1 - r_p r_m r_l} \tag{4.13}$$

which is a constant. The transfer function for the carrier fluctuations is a function of frequency,

$$T_{\delta a_{in}}(\omega) = -\frac{t_p t_m \mathrm{e}^{i\phi_v(\omega)}}{1 - r_p r_m r_l \mathrm{e}^{i2\phi_v(\omega)}} \tag{4.14}$$

here the round trip phase shift the fluctuations receive, $\phi_v(\omega) = \omega_v L/c$, which is dependent on the frequency relative to the carrier. As these two transfer functions are small the amount of carrier and carrier fluctuations that transfer to the output is small. As the off-

[3] derived in the appendix A

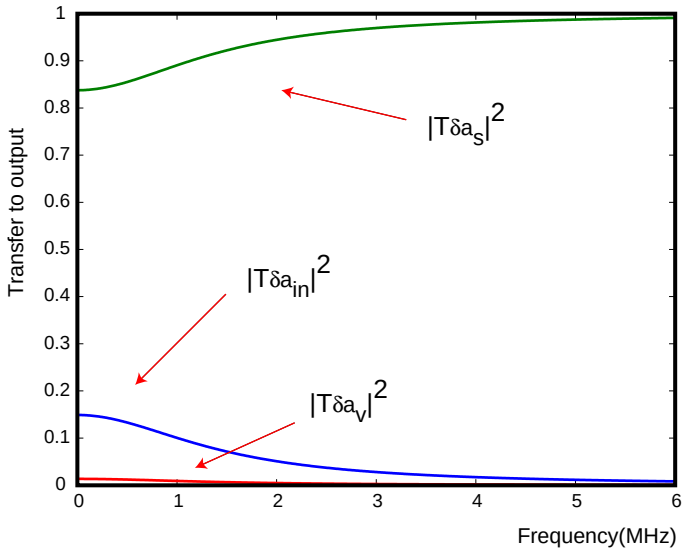

Figure 4.3: Plots of the magnitude of the transfer functions from each port of the cavity to the output of the interferometer.

set used to lock the interferometer decreases($r_m \to 1$) these transfer functions approach zero. The transfer function for the squeezing is,

$$T_{\delta a_s}(\omega) = \frac{r_m - r_p r_l e^{i2\phi_v(\omega)}}{1 - r_p r_m r_l e^{i2\phi_v(\omega)}} \tag{4.15}$$

which is generally close to unity as r_m is large. The transfer function of the vacuum is given by

$$T_{\delta a_v}(\omega) = -\frac{t_m t_l r_p e^{i\phi_v(\omega)}}{1 - r_p r_m r_l e^{i2\phi_v(\omega)}} \tag{4.16}$$

it is close to zero since the transmission of the loss mirror, t_l (equal to the losses inside the cavity)is small. The power magnitude of each transfer function is plotted as a function of frequency in figure 4.3 for typical experimental parameters($r_m = \sqrt{0.99}$,$r_p = \sqrt{0.9}$, $t_l = \sqrt{0.01}$ and $L = 1$m). The highest transfer function is from the squeezing port. It approaches 1 outside the cavity linewidth. Near resonance (DC) more of the carrier field fluctuations transfer to the output, replacing some of the squeezing. These transfer functions are strongly dependent on the Michelson reflectivity, r_m. For high transfer of squeezing to the output it is preferable to have $r_m \to 1$. The frequency dependent behavior shows that it the transfer function of the squeezing port is high far from the resonance of the cavity. Thus to reduce quantum noise below the shot noise limit improve the sensitivity of the interferometer it is preferable to operate outside the cavity linewidth.

4.3.3 The field at the output of the interferometer

The fields and respective transfer functions have been defined the behavior of the system can be analyzed. Taking the photon number at the output, with α as real, and discarding second order fluctuations terms,

$$\begin{aligned} n_{out}(\omega) &= \hat{a}^{\dagger}_{out}(\omega)\hat{a}_{out}(\omega) \\ &= T^2_{\alpha}(0)\alpha^2 + T_{\alpha}(0)T_{\delta a_{in}}(\omega)\alpha\delta\hat{a}_{in}(\omega) + T_{\alpha}(0)T_{\delta a_{in}}(\omega)\alpha\delta\hat{a}^{\dagger}_{in}(\omega) \\ &+ T_{\alpha}(0)T_{\delta a_s}(\omega)\alpha\delta\hat{a}_s(\omega) + T_{\alpha}(0)T_{\delta a_s}(\omega)\alpha\delta\hat{a}^{\dagger}_s(\omega) \\ &+ T_{\alpha}(0)T_{\delta a_v}(\omega)\alpha\delta\hat{a}_v(\omega) + T_{\alpha}(0)T_{\delta a_v}(\omega)\alpha\delta\hat{a}^{\dagger}_v(\omega) \end{aligned} \tag{4.17}$$

This can be simplified using Eulers equation, some factoring and the substitutions for $\delta X^{+}_{a}(\omega)$ and $\delta X^{-}_{a}(\omega)$. Then,

$$\begin{aligned} n_{out}(\omega) &= T^2_{\alpha}(0)\alpha^2 \\ &+ \alpha T_{\alpha}(0)T_{\delta a_{in}}(\omega)\left[\delta X^{+}_{in}(\omega)\cos\phi_{\delta a_{in}} + \delta X^{-}_{in}(\omega)\sin\phi_{\delta a_{in}}\right] \\ &+ \alpha T_{\alpha}(0)T_{\delta a_s}(\omega)\left[\delta X^{+}_{s}(\omega)\cos\phi_{\delta a_s} + \delta X^{-}_{s}(\omega)\sin\phi_{\delta a_s}\right] \\ &+ \alpha T_{\alpha}(0)T_{\delta a_v}(\omega)\left[\delta X^{+}_{v}(\omega)\cos\phi_{\delta a_v} + \delta X^{-}_{v}(\omega)\sin\phi_{\delta a_v}\right] \end{aligned} \tag{4.18}$$

Here the angles $\phi_{a_{in}}$, ϕ_{a_s} and ϕ_{a_v} define the phase difference of each of the fluctuations relative to α. The carrier and vacuum fluctuations have isotropic distribution of noise in amplitude and phase quadratures. Their phase relative to α is unimportant, as any projection of noise has the same cross section. Then for convenience, we choose $\phi_{\delta a_{in}} = \phi_{\delta a_v} = 0$, then the photon number simplifies to

$$\begin{aligned} n_{out}(\omega) &= \alpha^2 T^2_{\alpha}(0) + \alpha T_{\alpha}(0)\big\{T_{\delta a_{in}}(\omega)\delta X^{+}_{in}(\omega) + T_{\delta a_v}(\omega)\delta X^{+}_{v}(\omega) \\ &+ T_{\delta a_s}(\omega)\left[\delta X^{+}_{s}(\omega)\cos\phi_{\delta a_s} + \delta X^{-}_{s}(\omega)\sin\phi_{\delta a_s}\right]\big\} \end{aligned} \tag{4.19}$$

The first term in this equation is the DC power at the output. This is the LO for the Michelson, used for control and signal readout. The rest of the terms have fluctuations scaled by the carrier amplitude. The squeezing term (last term) is the dominant fluctuation term as the squeezing term, as $T_{\delta a_s}(\omega) \approx 1$. The quadrature of the squeezing fluctuations measured is phase dependent. This is important as one quadrature is squeezed and the other antisqueezed. To reduce quantum noise on the signal, the squeezed quadrature phase relative to the carrier should be set to zero. Therefore, either quadrature squeezing can be used to supress quantum noise, given that it has the correct relative phase. We use amplitude quadrature squeezing so we lock to $\phi_{\delta a_s} = 0$. A vector diagram of the fields is shown in figure 4.4. The two long vectors represent the fields in the Michelson arms, the phase difference between them couples the offset locking LO ($\alpha T_{\alpha}(0)$) to the output. A gravitational wave signal induces phase modulation of the two long vectors, and couples the signal in phase with the LO. The squeezing ellipse is set to minimize phase noise on the fields in the arms of the interferometer, which is in the amplitude quadrature of the signal. The large fluctuations are in the orthogonal quadrature are not measured.

The photodetectors are plugged into a spectrum analyzer. The spectrum analyzer measures the power spectrum of the photocurrent which is proportional to the variance

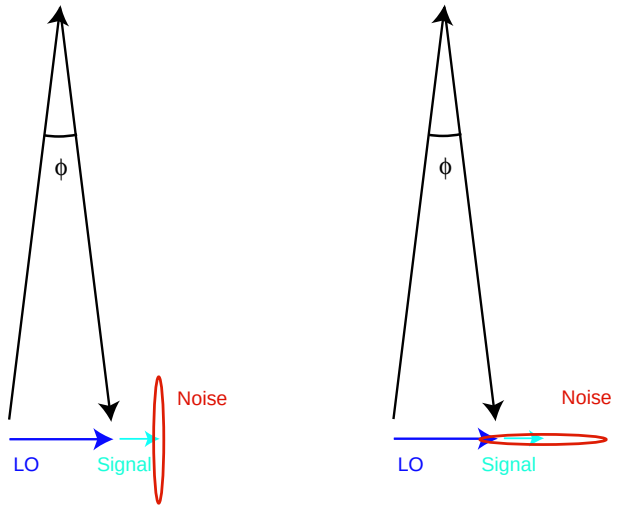

Figure 4.4: Vector diagrams of the fields in the Michelson arms and the resultant, the field coupled to the output. In (a) the orientation of the squeezed light has been shown to minimize the fluctuations on the signal. (b) shows incorrect orientation of the squeezing results in more fluctuations on the signal.

of the photocurrent. The variance of the field at the output is given by,

$$\begin{aligned} V_{out}(\omega) &= \langle (a_{out}^{\dagger} a_{out})^2 \rangle - \langle (a_{out}^{\dagger} a_{out}) \rangle^2 \\ &= \alpha^2 |T_\alpha(0) T_{\delta a_{in}}(\omega)|^2 \langle |\delta X_{in}^{+}(\omega)| \rangle^2 + \alpha^2 |T_\alpha(0) T_{\delta a_v}(\omega)|^2 \langle |\delta X_v^{+}(\omega)| \rangle^2 \\ &+ \alpha^2 |T_\alpha(0) T_{\delta a_s}(\omega)|^2 \left[\langle |\delta X_s^{+}(\omega))| \rangle^2 \cos^2 \phi_{\delta a_s} + \langle |\delta X_s^{-}(\omega)| \rangle^2 \sin^2 \phi_{\delta a_s} \right] \end{aligned} \tag{4.20}$$

The terms with the product of uncorrelated noises sources are on average zero and have been discarded. Rewriting this equation substituting in the variances of the each field,

$$\begin{aligned} V_{out}(\omega) &= \alpha^2 |T_\alpha(0) T_{\delta a_{in}}(\omega)|^2 V_{in}^{+} + \alpha^2 |T_\alpha(0) T_{\delta a_v}(\omega)|^2 V_v^{+} \\ &+ \alpha^2 |T_\alpha(0) T_{\delta a_s}(\omega)|^2 \left[V_s^{+} \cos^2 \phi_{\delta a_s} + V_s^{-} \sin^2 \phi_{\delta a_s} \right] \end{aligned} \tag{4.21}$$

To model our experiment we consider 3dB of input squeezing over the detection frequency range. Theoretical plots of the frequency spectra of the detected output variance for a simple Michelson and a power recycled Michelson (PRM) are shown in Fig.4.5. The results show improved performance of the PRM compared to the simple Michelson. This difference is a result of two separate effects. Firstly, to keep the same power at the homodyne photodetector, the position of the Michelson fringe changes, such that the effective Michelson reflectivity increases. In our experiment the reflectivity for the simple Michelson is $R_m \approx 0.92$, where as $R_m \approx 0.99$ for the PRM. The result is an increase in $T_{\delta \mathrm{a_s}}(\omega)$ and a decrease in $T_{\alpha(0)}(\omega)$, so that more squeezing is transferred to the interferometer output. In the presence of a power recycling mirror, therefore, less squeezing is wasted in the interferometer. Secondly, the power mirror introduces a frequency dependence to the squeezing transfer function, $T_{\delta \mathrm{a_s}}$. Outside the power cavity linewidth, the interferometer

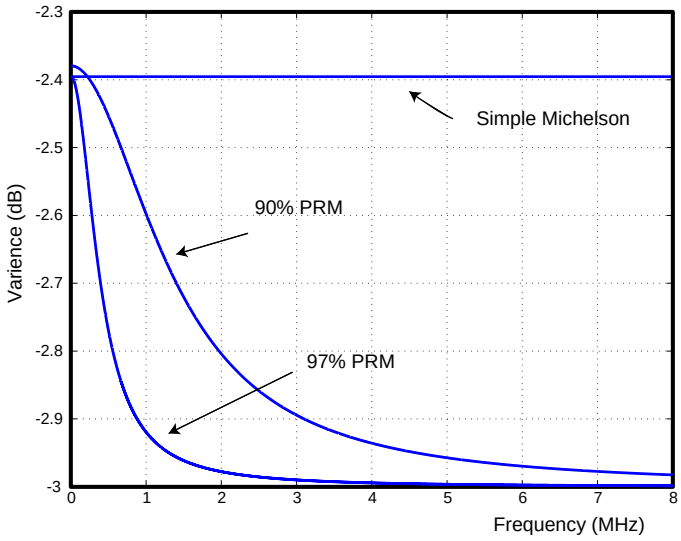

Figure 4.5: The variance of the output field of a Michelson and power recycled Michelson with 3dB of squeezed light added to the dark port. The variance for the with simple Michelson case (no power mirror) sits at -2.4 dB and displays no frequency dependence. The power recycling cases have a distinct frequency dependence due to the linewidth of the power recycling cavity. The variance out improves as the frequency is further from resonance since the cavity reflectivity increase, reflecting more squeezing.

becomes highly reflective so that transfer of the squeezing becomes close to ideal.

4.4 Chapter summary

This chapter has introduced a theoretical model of the power recycled Michelson interferometer with squeezing. This has been presented using linearized operators and the transfer function approach. It has described the source of shot noise in the interferometer and how to minimize it. Theoretical predictions of the operation of the interferometer with squeezing have been calculated for comparison to experimental data in chapter 6.

Chapter 5

The Experiment

5.1 Overview

This chapter describes the experimental setup of the PRM with squeezing. The first part of the chapter introduces the laser and the preparation of the laser light for the PRM. Then the techniques used to generate a signal, in order to characterize the interferometer, and the method to inject the squeezing into the interferometer are presented. The last part of this chapter is concerned with the optical and control configurations. The optical layout for the PRM with squeezing and the squeezer are discussed separately before the control of both systems is presented.

5.2 The laser

The laser is a Nd:YAG non planar ring oscillator with maximum output power of 700 mW at $\lambda = 1064$ nm. It operates at a single frequency with a slightly elliptical spatial mode output similar to the TEM_{00}.

The light from a Nd:YAG laser has large classical intensity noise from DC to around 100 MHz due to the relaxation oscillation(RO) [30]. RRO intensity noise arises from the coupling of energy back and forth from the lasing atoms to laser radiation. In Nd:YAG lasers the RO resonance frequency is typically around 500 kHz where there is a large intensity noise spike up to 10^8 times larger than the SNL. The classical intensity noise rolls off at higher frequencies until it reaches the SNL at around 10MHz. The phase noise of a laser is typically larger than the intensity noise. This however, is common to all beams and is cancelled out on interference to the extent that it is difficult to measure.

The frequency of the laser light can be controlled (varied) in the slow and fast regimes to maintain lock with the modecleaner. The lasing crystal sits on a peltier element and a piezo electric transducer (PZT) is bonded onto it's upper surface in order to change the crystal length and therefore the lasing frequency. The peltier element heats or cools the crystal, producing a large dynamic range (order of several GHz) at bandwidth of $\sim$100mHz. The PZT bonded to the lasing crystal stresses the crystal and has a smaller dynamic range (order of 50MHz) at a higher bandwidth of up to $\sim$200kHz.

5.3 Preparation of the light

The laser does not produce an ideal state of light. For the squeezer and the carrier field in this experiment, we require SNL TEM_{00} light with the desired polarization and mode

size. The laser light is conditioned to achieve this before it enters the PRM. This section describes the techniques used to prepare the light.

5.3.1 The modecleaner

The laser light is transmitted through a modecleaner before incidence on the PRM. The modecleaner performs two important operations: It filters high frequency intensity and phase noise and it defines a high quality TEM_{00} spatial mode.

This experiment requires SNL light at around $f = 5$ MHz in order to get below the SNL by use of squeezing. The modecleaner used in this experiment is a Fabry Perot ring cavity with linewidth, $l \sim 2$ MHz[1]. The transfer function on transmission is equivalent to a low pass filter (LPF). Noise sidebands outside the modecleaner linewidth are removed, leaving the laser light classical noise only at low frequency. The transmitted light reaches the SNL at a frequency around 4 times the cavity linewidth.

The squeezed light comes from a cavity (the OPA) and therefore has the well defined TEM_{00} spatial mode of this cavity. For high interference efficiency the carrier must be in the same spatial mode as the squeezed light. The modecleaner ensures the spatial purity of the carrier as it forced to resonate only the TEM_{00} mode; all higher order modes being rejected by the cavity.

5.3.2 Mode-matching

While both the OPA and the modecleaner cavities produce TEM_{00} modes, these modes must be transformed to ensure that they are spatially identical at the point of interference.

In this experiment the squeezed light and the carrier modes are matched to the PRM cavity mode for high coupling efficiency. The match of the squeezed light to the PRM cavity is particularly important as the interference with the carrier field takes place inside the PRM cavity. Bad mode-matching gives poor fringe visibility and therefore poor squeezing detection efficiency(see equation 3.27). The carrier field mode-matching into the PRM cavity is less important, mismatch results in less field coupling into the cavity, reducing only the DC power in the cavity. Mode-matching is also performed for the measurement of the squeezing on the homodyne configuration. In this case the squeezing mode is set to match the local oscillator.

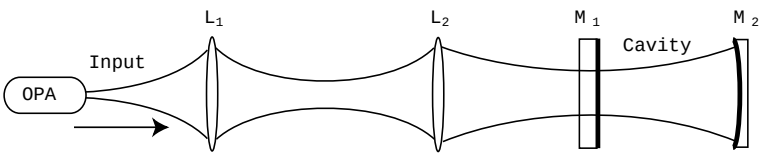

Figure 5.1: Mode-matching the squeezed beam to the power recycled Michelson cavity. Lens focal length and separations are adjusted to produce the required mode that is resonant in the cavity.

The modes supported by a cavity depend on the separation and curvature of the mirrors. The PRM cavity has a flat power mirror (radius of curvature, $R = \infty$) and Micheslon arm mirrors with $R = 1.5$ m. For the cavity to be stable the length from the

[1]The modecleaner was setup by B. Buchler previous to the start of this experiment. Full specifications to be found in [27]

power mirror to the Michelson arm mirrors, L is required to be less than or equal to the radius of curvature of the curved mirrors ie $L \leqslant R$. We choose $L_{prm} = 1$ m. The mode shape of the cavity[2] has the waist at the flat power mirror and wavefront curvature equal to the arm mirror curvature at the Michelson arm mirrors. This is shown schematically in figure 5.1. The incident mode shape is adjusted using lenses to match this shape when it enters the cavity. This is achieved to high precision by measuring the beam size and manipulating it using lenses until the incident field matches the calculated cavity mode.

5.3.3 Polarization optics

Polarization optics are used to match the polarization state of the squeezed and carrier fields at interference. The injection of squeezing into the interferometer uses polarization optics discussed in the following section. The polarization optics used in the experiment are:

· $\frac{\lambda}{2}$ plate. This rotates the linear polarized component of the light by up to 90^0.

· $\frac{\lambda}{4}$ plate. This imparts a phase shift between the orthogonal polarizations thus changing linear polarized light to circularly polarized or vise versa. The combination of the two wave plates can transform any polarization state to any other.

· Polarizing beam splitter (PBS). This beamsplitter separates the polarization. components of light by transmitting horizontal and reflecting vertical.

· Faraday rotator. This consists of a crystal that exhibits the Faraday effect with a static magnetic field applied along the optical axis. The polarization state of light transmitted in either direction through the rotator is rotated in the same direction. The applied magnetic field can be manipulated to give a 45^0 rotation upon transit of the rotator. For example, on double pass a vertically polarized beam is transformed to horizontal polarization. (In contrast, the double pass polarization shift of a $\frac{\lambda}{2}$ plate to a linear polarization state is zero. The polarization shift in one direction is exactly undone by the opposite imparted in the other direction.)

· A Faraday isolator is made up of a PBS on each end of a Faraday rotator. One PBS is 45^0 to the horizontal, thus transmitting 45^0 linear polarized light. It isolates a component from reflections travelling back toward it, by allowing light to pass though one way only. Isolators are used in front of lasers in order to prevent optical feedback. In this experiment an isolator is used to inject squeezed light into the interferometer as discussed in section 5.4.2.

5.4 Experimental techniques

In this section the technique used to generate a signal in order to characterize our interferometer and the method used to inject the squeezed light into the interferometer are described.

5.4.1 Signal generation

An RF sinusoidal voltage is applied to one Michelson arm mirror PZT which modulates the arm length. This produces a signal used to characterize the interferometer similar to

[2]Calculated using the computer program ABCD

the effect of a gravitational wave (orders of magnitude larger). The RF signal is used instead of a real gravitational wave detection signal frequencies (10's Hz - 10 kHz) because of the scaling required from the bench top to long baseline interferometers.

The signal frequency, $f_{sig} = 5.46\text{MHz}$ is chosen after searching the PZT response for a mechanical resonance around the optimal squeezing frequency ($\sim 5\text{MHz}$). The signal frequency is well outside the usual PZT operating bandwidth and the amplitude response is poor. To find the signal we locked the PRM and applied a signal to the PZT and looked at a spectrum analyzer output. The interferometer is quite sensitive, and we found many such signals.

5.4.2 Squeezed light injection optics

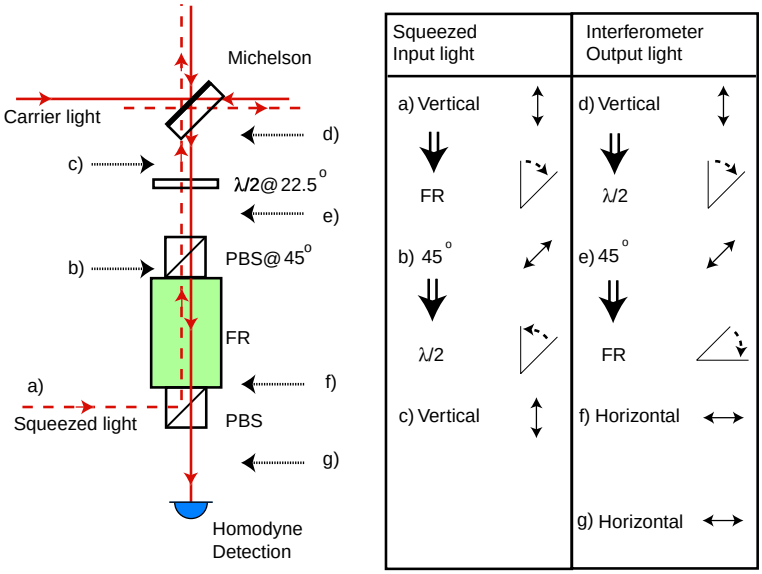

Figure 5.2: The polarization states of the light as it passed through the Faraday isolator.

A Faraday isolator (Gšanger FR 1060/5) is used to inject the squeezing into the dark port of the Michelson beamsplitter. With this method the standard configuration for GW detectors is maintained and the readout is unaffected.

The figure 5.2 shows the polarization states of the light as it enters and passes through the isolator. The input and output light is shown to be spatially separated for clarity, however in the experiment they overlap. The squeezed light has linear vertical polarization when it exits the OPA. It is incident and reflects off the first PBS of the isolator into the rotator. Here the polarization is rotated by 45^0. Then it is transmitted through the PBS@45^0. The light then passes through a $\frac{\lambda}{2}$ plate set at 22.5^0 which rotates the polarization back to vertical. The squeezed field then interferes with the carrier field (also in the vertical polarization) inside the Michelson. Part of the carrier field, now with the squeezed noise sidebands exits to the homodyne detector. It passes through the $\frac{\lambda}{2}$ plate changing the polarization to linear 45^0. It is transmitted through PBS@45^0 then passes through the rotator, receiving a further 45^0 polarization shift, leaving the polarization state in horizontal. This is transmitted through PBS out to the homodyne detection.

5.5 Optical Layout

The optical and control configurations for the PRM were decided on before we started to build the configuration in the lab. The squeezer was already built up and was operational prior to this experiment.

5.5.1 Discussion of the optical layout

A schematic of the optical layout for the power recycled Michelson with squeezing is shown in figure 5.3. The carrier and squeezed fields optical path will be introduced separately before the combination is discussed.

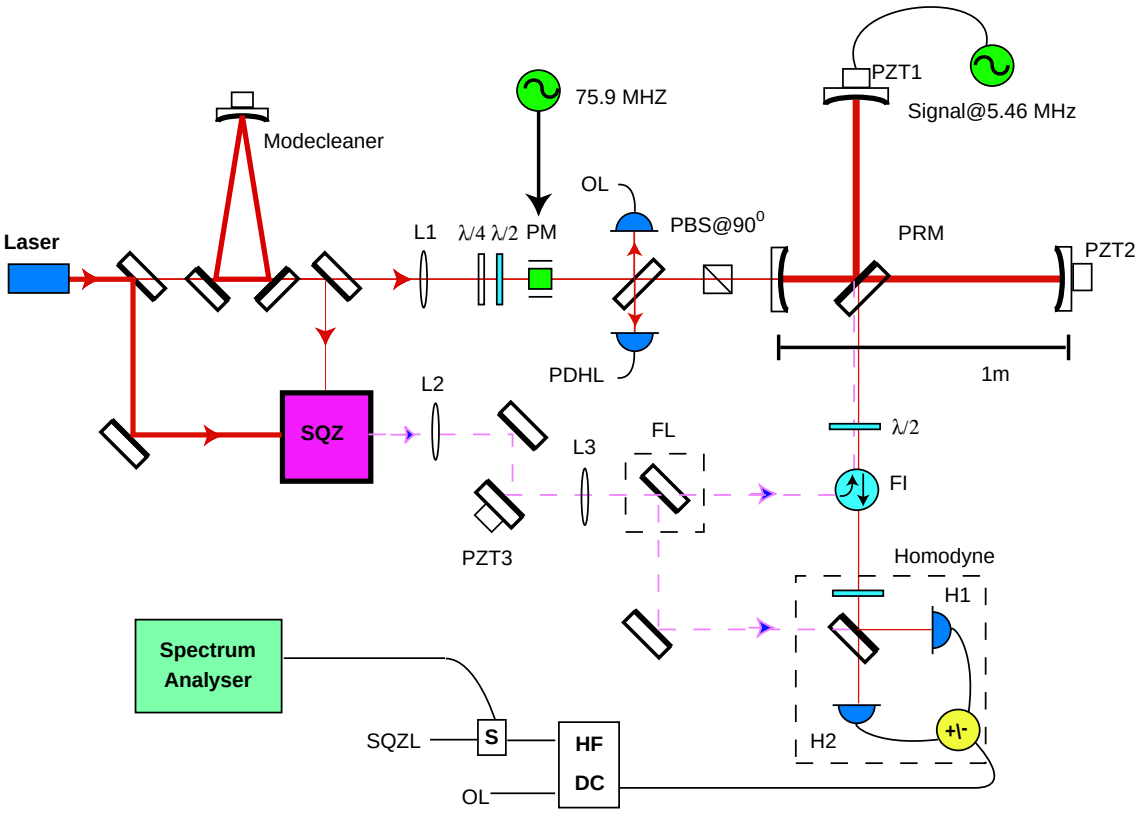

Figure 5.3: Schematic of the experiment. The laser light passed through a modecleaner is divided for the squeezer and the PRM. Squeezed light can either be injected into the output port of the interferometer using a Faraday isolator or interrogated using a homodyne detection system with a flipper mirror. L1,L2,L3 =Modematchig lenses. $\lambda/4$, $\lambda/2$ = Waveplates, FL=flipper mirror, FI = Farraday isolator OL=offset locking detector, PDHL=PDH locking detector, H1, H2 = Homodyne photo detectors, PZT=piezo-electric transducer PM=Phase modulation and SQZ=squeezed state generation system.

Carrier field

Approximately 20mW of the laser light transmitted through the modecleaner is directed towards the PRM. It passes through a mode-matching lens (L1) and polarization optics

adjusting the light's polarization state to linear vertical. It passes through a phase modulator (PM) which introduces PM sidebands at the modulation frequency $f_m = 75.9\text{MHz}$. A tap off of the beam is measured on a photodetector (OL) used for the differential mode Michelson locking loop. The light is then transmitted through a PBS@90^0 to insure only vertical polarization is incidence on the PRM.

Both the differential mode of the Michelson and the power recycling cavity are locked and the power builds up with in the PRM. Light that is reflected from the front of the PRM is detected on a high speed photodetector (PDHL) and used for PDH locking of the power recycling cavity. The offset locking technique requires the differential mode of the Michelson to be locked to a point slightly to one side of the dark fringe. This couples some of the circulating light to the output of the interferometer. This light passes through a $\lambda/2$ plate and a Faraday isolator before it is detected on the homodyne detection system. For operating the PRM the sum of the two detectors (H1+H2) is taken which is equivalent to having a single detector[3]. The DC voltage taken from the homodyne is used for the offset locking (OL). The high frequency component (RF signal) is split into two outputs with one output used to lock the squeezing phase (SQZL) while the other is viewed directly on a spectrum analyzer.

Squeezed light in the locked PRM

The squeezing passes though the isolator and into the interferometer. It is incident on the dark port of the Michelson beamsplitter where it interferes with the carrier field. The small amount of the carrier coupled to the output has squeezed noise. The noise on the output field is measured on the spectrum analyzer by taking the sum of the homodyne detectors (H1+H2). The squeezing phase is scanned by applying a sinusoidal signal to PZT3. The squeezing is locked with relative phase to the carrier output such that the minimum projection of the squeezing ellipse measured. This gives the local oscillator the noise characteristics of the squeezing, improving the sensitivity of the interferometer.

When the PRM and squeezing are locked, a test signal is applied to one of the Michelson arm PZT's at $f_{sig} = 5.46\text{MHz}$. The results are taken on the spectrum analyzer.

The squeezed field measurements

The squeezing is measured on the homodyne detector before it is injected into the PRM. It is redirected using the flipper mirror (FL) and incident on the homodyne configuration setup at the the output of the PRM. The output field from the PRM is used as the local oscillator. The subtraction of the photodetectors(H1-H2) is taken and viewed on the spectrum analyzer. The squeezing phase can be locked or scanned by applying a signal to PZT3 whilst the parameters of the squeezer are adjusted to improve the amount of squeezing.

5.5.2 The optical layout of the squeezer

The squeezer was already built prior to the commencement of this research with full specifications to be found in [27]. A schematic of the squeezer setup is shown in figure 5.4. Most of the laser light (∼500mW) is used in the SHG to produce the pump@532nm (∼220mW) for the OPA. The pump passes out of the SHG and reflects off the dichroic

[3]This is if the other input of the beam splitter is vacant. See section 3.7.2

mirror (DC1) (transmissive to 1064nm and highly reflective to 532nm). This is directed to the OPA off a mirror mounted on a PZT, through a second dichroic mirror (DC2) (transmissive to 532nm and highly reflective to 1064nm) and into the front of the OPA. The OPA has reflectivities on the front and back mirrors of 95.6%/4% and 99.96%/99.96% for 1064nm and 532nm respectively. The pump therefore performs a double pass of the OPA.

The seed for the OPA comes from a tap off after the modecleaner, as SNL light is required to produce squeezing. It is transmitted into and resonates in the OPA, where if the phase matching is correct the optical parametric process takes place[4]. The squeezed light then exits through the front of the OPA and reflects off the dichroic mirror (DC2) towards the PRM. The type of squeezing produced, (amplitude or phase) is determined by the phase of the pump relative to the seed. This is controlled by a PZT in the pump path.

The OPA is a monolithic $MgO : LiNbO_3$ crystal 7.5 mm in length. The OPA temperature is controlled to obtain the phase matching condition. Since the OPA is monolithic, it has no means of length control, so the laser is locked to it. The crystal has a phase modulation voltage applied across it. This imparts PM sidebands on the reflected and transmitted fields. Thus the squeezing field has the PM sidebands that are used to lock it to the PRM.

The SHG is a hemilithic cavity $MgO : LiNbO_3$ crystal with one high reflective mirror coating and an output coupler with 94%/4% for 1064/532nm reflectivity mounted on a PZT actuator. The SHG is also temperature controlled for phase matching and has phase modulation voltage applied to it used for locking purposes.

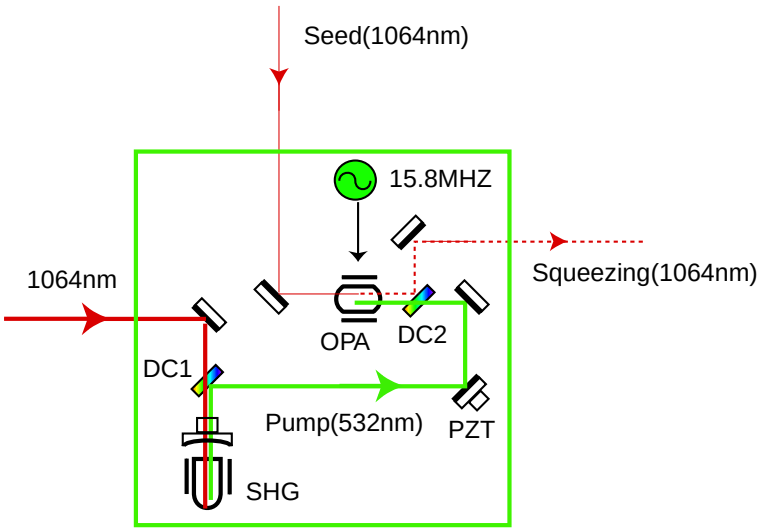

Figure 5.4: A schematic of the squeezer. DC1, DC2 = Dichroic mirrors.

5.6 Control

The control scheme for the squeezer relies on having the laser locked to the OPA resonance frequency since it is monolithic. Thus the power recycled Michelson must be locked to the laser frequency rather than vise versa. The control scheme for this entire

experiment is quite elaborate. The PRM requires three length degrees of freedom locking loops and the squeezer requires another four. Seven length degrees of freedom are controlled as the acoustic and thermal disturbances conspire to push the cavities off resonance.

5.6.1 Control of power recycled Michelson with squeezing

The three degrees of freedom that need to be controlled in a PRM with squeezing are the power recycling cavity, the differential mode of the Michelson and the phase of the squeezed field relative to the carrier. Schematics of each locking loop are shown in figure 5.5.

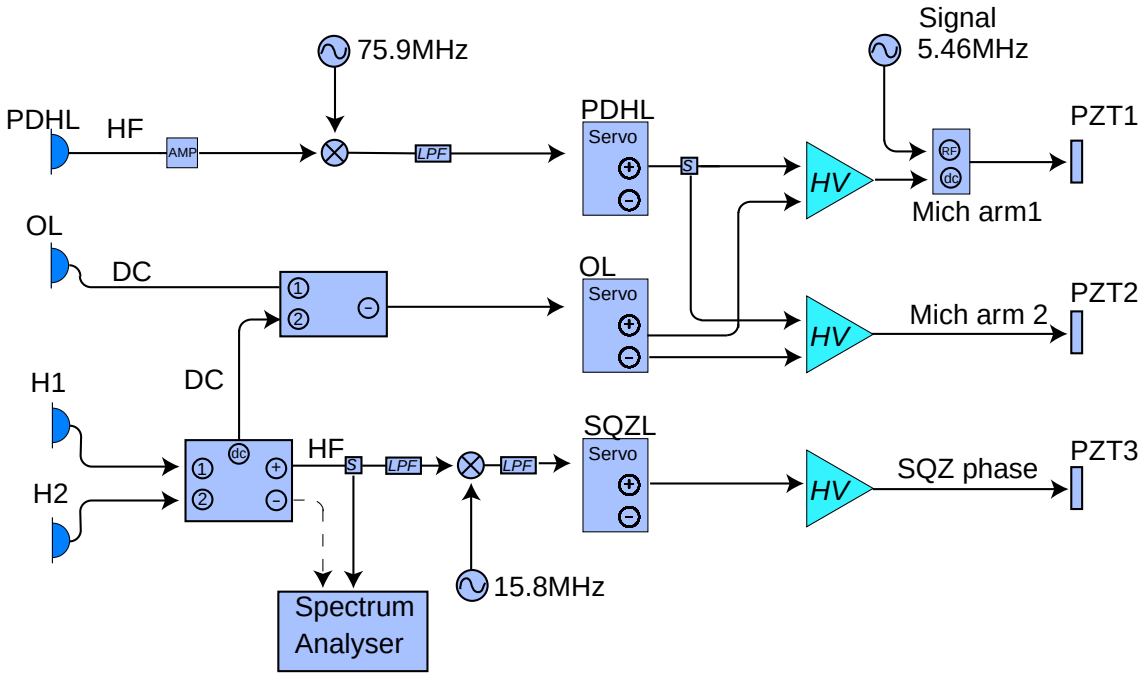

Figure 5.5: The three control loops of the PRM with squeezing. The output of the photodetectors, also shown in figure 5.3, are conditioned to extract error signals, then fedback to the interferometer via PZTs. PDHL=PDH locking photodetector, OL = Offset locking photodetector, H1, H2 = Homodyne photodetectors, HF= High frequency, HV = High voltage amplifier, PZT=piezoelectric transducer

The power recycling cavity

The power recycling cavity is held on resonance with the laser frequency using PDH locking. The carrier field has sidebands at 75.9 MHz imposed on it by a phase modulator. The field reflected from the PRM is detected on a high speed photodetector (PDHL). This contains a DC component plus a RF component at 75.9MHz. The RF signal from the photodetector is firstly amplified then demodulated with a local oscillator signal. The relative phase of RF signal and the local oscillator is adjusted using different cable lengths so that the in-quadrature error signal is demodulated. The error signal, now at DC, is low pass filtered to remove the high frequency components introduced in demodulation. The

error signal is fed into the common mode (PDHL) servo. The positive output of the servo is split into two and fed into the both Michelson arm mirror PZT's high voltage amplifiers. This changes both PZT's by the same amount thus changing the average length of the Michelson, and therefore the power recycling cavity length in order to maintain lock.

The differential mode of the Michelson

The differential mode of the Michelson is controlled by offset locking. A DC offset obtained optically before the PRM on the photodetector (OL) , is subtracted from the DC voltage measured at the output of the homodyne photodetectors (H1,H2). This creates an error signal which is fed into the differential mode (OL) servo. The positive and negative outputs of the servo then drive the different Michelson arm mirror PZT's high voltage amplifiers. The different polarities of the signals changes the differential length of the Michelson arms to maintaining the desired operating point on the Michelson fringe.

The squeezed light phase in the PRM

After the power recycling cavity and differential mode of the Michelson are locked up, the squeezed field is injected to the dark port. The relative phase is locked using PDH locking. The squeezed field has very low coherent amplitude ($\sim$30 μW), which carries PM sidebands at 15.8 MHz. The error signal is read out from the high frequency component of the sum of the homodyne photodetectors at the output. This is demodulated, low pass filtered and fed into the squeeze servo. The signal out of the squeeze servo is amplified and then fed into the PZT on the squeezing path to the interferometer.

The squeezed light measured by the homodyne detector

The squeezing phase is locked to the local oscillator much like it is to the power recycling cavity.

5.6.2 Gain estimates

The locking of each loop requires the correct gain. To lock a system with many parameters such as the power recycling cavity, estimates for the required gain are essential. Estimates are made by modelling each of the cavity and the power cavity and differential mode of the Michelson error signals. A comprehensive MATLAB code used to perform this gain estimate can be found in the appendix C.

5.6.3 Control of the squeezer

Since the OPA is monolithic and has no means of fast length control the laser must be locked to it. This is done indirectly as the seed for the OPA first passes through the modecleaner. The order for locking the squeezer is the following,

· The laser to the modecleaner, using tiltlocking[31],
· The modecleaner (and indirectly the laser) to the OPA using PDH locking,
· The SHG to the laser, using PDH locking and
· The pump from the SHG to the OPA, using PDH locking.

5.7 Electronic equipment

The control electronics used in this experiment are mainly custom items built in-house at ANU over the last 10 years. The main elements are the servo mechanisms and piezo-electronic transducers. The photodetectors are also custom makes, built prior to the commencement of this research.

Servos

The servo mechanisms are used to filter and prepare the raw error signal before it is fed into the PZT's. The servos used in this experiment are built to perform high gain at low frequencies with a sharp drop of gain at the PZT resonant frequency. This is done using a third order elliptic filter with the first zero coinciding with the PZT resonant frequency. It allows high gain to control acoustic disturbances (low frequency) without sending signal to the PZT at its resonance frequency. The frequency response of the servos is shown in appendix D.

Piezo-electric transducers

The two Michelson arm mirrors are mounted on PZT actuators which deliver fast length control to the PRM. A PZT is located in the squeezing path to control the relative phase of the squeezed light to the carrier light.

When a voltage is applied to a PZT it expands or contracts($\sim 1\mu\mathrm{m}$) depending on the voltage magnitude and sign. A PZT can be used to control the frequency range from just above DC to near the resonance frequency at $\sim$ 10 kHz. The response drops of dramatically at higher frequency. The amplitude and phase response of the PZT's used on the Michelson arm mirrors is shown in appendix D.

Photodetectors

The homodyne photodetectors were built around the EXT500 photodiode specifications and circuit diagrams can be found in [32]. The photodetector used for power recycling cavity PDH locking is a custom built detector with response suited to the modulation frequency with specifications [32]. It has HF and DC outputs used for the error signal and DC power measurements respectively. The specifications for the photodetector used for offset locking can be found [33].

Adder/Subtractors

The active adder/subtractor used for the Homodyne is custom built with specifications [27]. It provides HF ($\sim$ MHz) addition and subtraction and a DC output making this ideal for both RF signal readout and locking, and offset locking at DC.

We used a passive adder/subtractor for the calibration of noise on the carrier with shot noise.

The adder/subtractor used for offset locking is a Stanford Research systems low noise pre-amp.

Bias T piece

A 'bias T' piece is used before one Michelson arm mirror PZT to combine the high voltage error signal (f<10kHz) and the mock GW signal (5.46MHz).

5.7.1 Total experiment

The total experiment including the squeezer and control is shown in figure 5.6. The left half of the bench is occupied by the squeezer and the right half is occupied by the PRM experiment. The complete control system is also shown.

5.8 Chapter summary

In this chapter the experiment has been described. The method for preparation of the input light, the squeezed light injection optics and signal generation have been discussed. The optical layout, the readout of the results and the control of the system has been presented in detail.

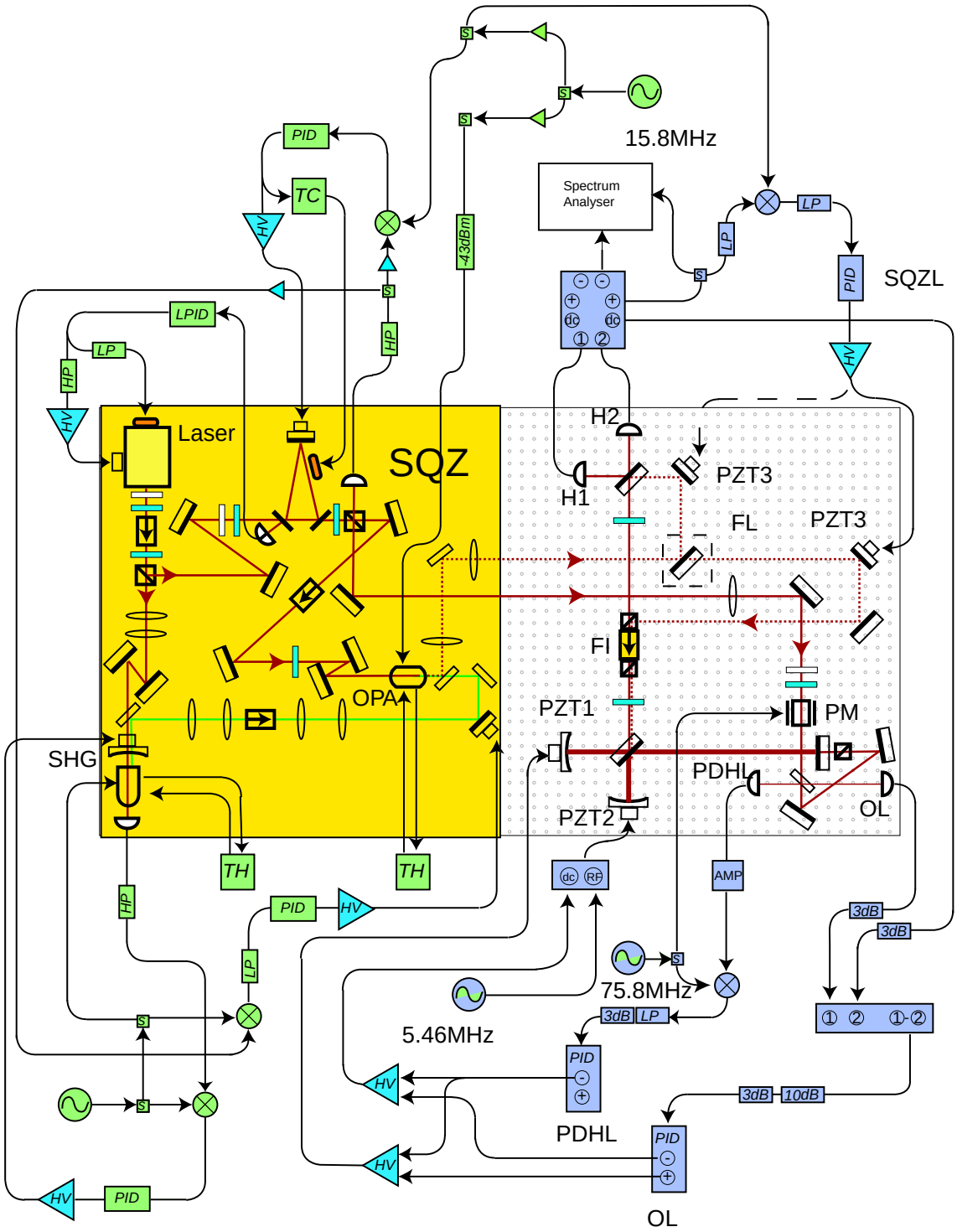

Figure 5.6: A detailed diagram of the total experiment. PDHL=PDH locking photodetector, OL = Offset locking photodetector, H1, H2 = Homodyne photodetectors, PID=Servos, HV = High voltage amplifier, PZT=piezo-electric transducer, FL=flipper mirror, FI = Farraday isolator, TH = thermal control, SQZ = squeezer

Chapter 6

Experimental Results

This chapter presents the results from the first experimental demonstration of an interferometric gravitational wave detector configuration that was operated below the shot noise limit. An improvement in the signal-to-noise ratio of 2.3dB was measured and the interferometer locked stably for over 15 minutes.

Section 6.1 presents measurements of the initial parameters that were required to operate the PRM below the shot noise limit and characterize it. We report the results of the intensity noise on the carrier and the squeezed light before it was injected into the PRM. We demonstrate the stability of the signal that was used to measure the power recycling factor.

In section 6.2 the power recycling factor, the inferred intra cavity PRM loss and loss of the isolator used for injection of the squeezed light are presented.

In section 6.3 the results of the signal measurements using the PRM with and without squeezing are presented. The results are compared with the modelled predictions and the lock stability is measured.

Finally a comparison of the PRM with different power mirror reflectivities is made.

6.1 Initial parameters

The demonstration of the PRM below the SNL requires the following parameters;

· Shot noise limited carrier light at the signal frequency.

· Squeezed light.

· A signal for the characterization of the interferometer at a frequency outside the PRM cavity linewidth.

The measurements taken to demonstrate these parameters are presented in this section.

6.1.1 The carrier noise measurement

At the signal frequency the carrier light is required to be shot noise limited. The addition of squeezed light then enables the system to be operated below the SNL.

The spectrum of the carrier intensity noise can be compared with shot noise to determine the frequency at which it reaches the SNL. The measurement of the carrier light is performed using the standard homodyne configuration after transmission through the modecleaner. The sum of the photocurrents gives the intensity noise on the carrier light;

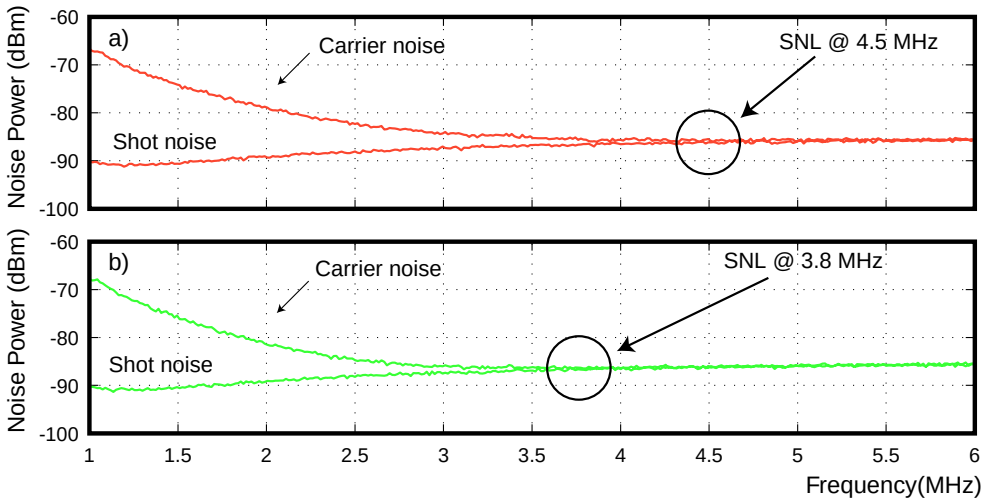

Figure 6.1: The carrier light intensity noise and shot noise spectra out of the modecleaner before the PRM. The electronic noise floor lies at -95dB. Resolution bandwidth (RBW) = 68kHz, Video Bandwidth (VBW) = 51Hz

the difference of the photocurrents gives the SNL[1].

Figure 6.1 a) shows the carrier intensity noise and shot noise from $1 - 6\mathrm{MHz}$[2]. The intensity noise reaches the SNL at $f_{snl} \approx 4.5\mathrm{MHz}$. The figure 6.1 (b) shows the intensity noise on the carrier after transmission through the PRM with a 90% reflectivity power mirror. The carrier is SNL at $f_{snl} \approx 3.8\mathrm{MHz}$. The carrier reaches the SNL at a lower frequency as more intensity noise is removed on transmission through the PRM, as it acts as a further modecleaner. These measurements indicate that to operate the PRM below the SNL the frequency chosen should be above 4.5MHz.

6.1.2 Measurement of the squeezed light

The squeezed light was measured before it was injected into the PRM for comparison of results taken after the PRM.

The squeezed light is measured using the standard homodyne configuration at the output of the PRM. The squeezed light is directed into the homodyne using the flipper mirror and the local oscillator is provided by the field transmitted through the PRM.

The figure 6.2 (a) shows the measurement of the squeezing noise at 5.5MHz. The flat trace shows the shot noise at $\approx -77.3 \pm 0.2\mathrm{dBm}$. The curved trace is the projection of the squeezed noise ellipse as the relative phase of the squeezing and local oscillator is varied. The maximum noise, at $\approx -66\mathrm{dBm}$, is the projection of the anti-squeezed quadrature. The minimum noise $-80.6 \pm 0.2\mathrm{dBm}$ is a projection of the squeezed quadrature which is $3.3 \pm 0.2\mathrm{dB}$ below the SNL.

The phase difference of the squeezed light and local oscillator was locked to show the spectrum of the squeezing. Figure 6.2 (b) shows the spectrum of the squeezing from 3-10MHz. In this spectrum the frequency response of the electronics (photodetectors,

[1]This calculation is shown in section 3.7.2. When only one input of the homodyne is filled with coherent light (the carrier) the vacuum is incident in the other port.

[2]The shot noise trace is curved due to the photodetector frequency response

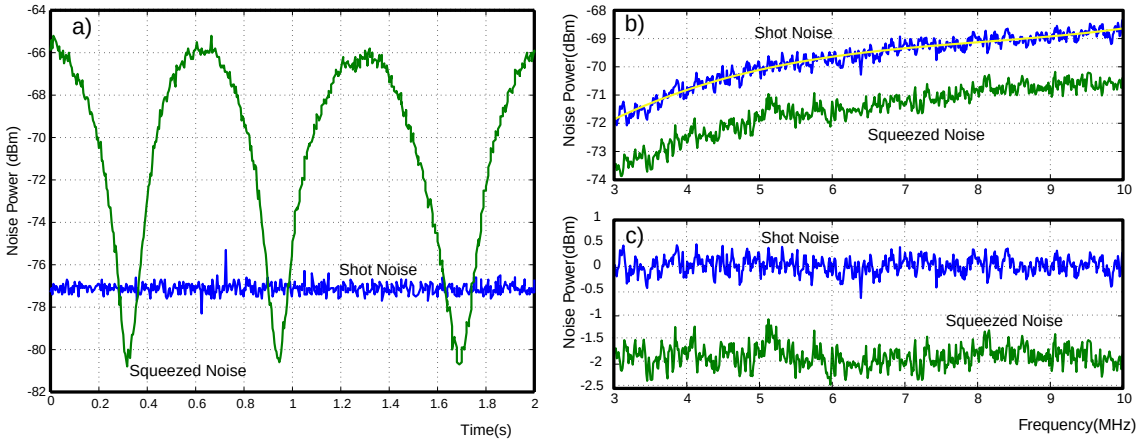

Figure 6.2: a) Scan of squeezing and shot noise at 5.5 MHz measured before the interferometer by homodyning; b) Locked squeezing and shot noise across 3-10MHz. c) Locked squeezing and shot noise across 3-10MHz with the electronic frequency response in b) normalized off. Electronic noise lies at -84.9dBm and the fringe visibility is measured at 97%. a) RBW = 100kHz, VBW = 300Hz. b) and c) RBW = 30kHz, VBW = 220Hz

adder/subtractor) imparts a common curved shape to the shot noise and squeezed noise. In Figure 6.2 (c) the common shape is removed by fitting a curve to the shot noise, and using this as the reference for shot noise. The squeezing is approximately 2dB below the SNL across the spectrum. The reason for the reduction in squeezing from 3.3dB to 2dB is thought to be poor homodyne efficiency on the second data run. Also, due to the experimental complexity of the squeezer the amount of squeezing produced and measured can vary on each data run.

These results can be compared to the squeezed light after interaction with the PRM, thereby allowing analysis of the PRM behavior

6.1.3 Signal

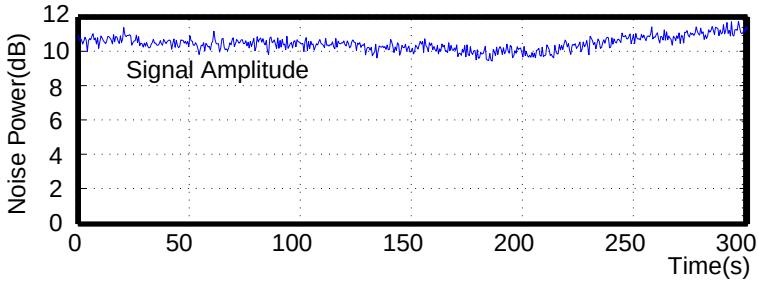

Figure 6.3: The signal power measured by locked 97% PRM for 5 minutes. Taken at 5.48 MHz zero frequency span.

A modulation signal was applied to one Michelson arm mirror PZT to simulate the

effect of a GW signal[3]. The signal measured at the output of the PRM was used to study the interaction of squeezing and power recycling.

The signal frequency was chosen to satisfy four conditions. The first condition was to be outside the PRM cavity linewidth ($\sim$ 2.5MHz) which is comparable to long base line GWD[4]. Secondly, a frequency where the carrier is SNL($>$ 4.5MHz). The third condition was at a frequency where squeezed light was optimal. The final condition satisfied was to be at a frequency where a mechanical resonance of the PZT could be found.

A mechanical resonance of the PZT is found at 5.46MHz which satisfies all four conditions. However it is well outside the designed operational bandwidth[5]. The signal amplitude was therefore analyzed over time to determine its stability. The signal power is plotted in figure 6.3 over a period of 5 minutes taken with zero frequency span. The measurement was read out from the output of the locked PRM with a 97% power mirror. The signal power over 5 minutes is,

$$Amp \quad = \quad 10.5 \pm 0.7\text{dB} \tag{6.1}$$

The variation in signal power was possibly due to thermal fluctuations in the laboratory. The properties of the PZT crystal may change with changing temperature, therefore the mechanical resonance frequency may change causing a different amplitude response to the modulation.

In this section we have demonstrated measurements of the initial parameters that are required to perform the PRM below the SNL and to analyze its behavior.

6.2 Power recycling factor and losses

This section reports the results of the power recycling factor of the PRM with a 90% reflectivity power mirror and the losses to the squeezed light when it was transferred to the PRM.

Given the squeezed light before the PRM and the measured losses on transfer, we can predict the result after the PRM with modelling and compare this to the results taken after the PRM.

6.2.1 Power recycling factor

The power recycling factor was obtained by comparison of the signal power at 5.46MHz measured with the simple Michelson (no power recycling) and the PRM with a 90% reflectivity power mirror.

The power recycling factor is directly proportional to the PRM intra cavity power. The power of the signal is determined by the intra cavity power. Therefore the ratio of the measured PRM signal power to the simple Michelson signal power gives the power recycling factor.

[3] A GW signal modulates both arms differentially. Since we modulate only one arm there is a negligible component of common phase shift.

[4] GW signals are expected between 40 Hz and a few KHz, which is outside the linewidth of power cavity for long baseline interferometers. Since this is a small scale prototype we simulate a signal a MHz.

[5] The operational bandwidth is approximately DC to 20 kHz. The measured PZT frequency response is shown in appendix D

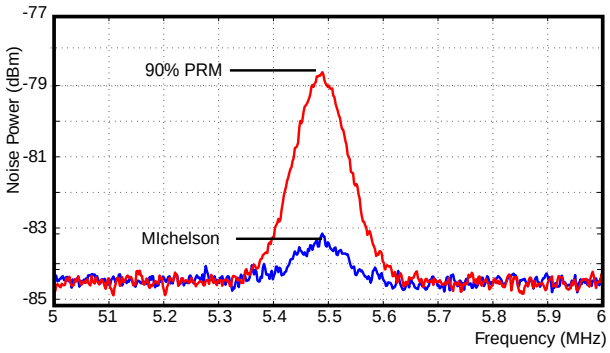

Figure 6.4: The power recycling factors for the 90% PRM can be calculated from the signal power measured by each configuration. Electronic noise lies at -93.5dBm, RBW = 100kHz, VBW = 30Hz.

The figure 6.4 (a) shows the signal measured by the simple Michelson and the PRM with a 90% reflectivity power mirror. The power recycling factor measured was,

$$F_{90\%} = S_{PRM}/S_{SM} \tag{6.2}$$
$$= 9.4 \pm 0.9 \tag{6.3}$$

where the error was implied from the signal stability measurements. This measurement was taken with Michelson fringe visibility of 99%.

6.2.2 PRM intra cavity losses

The PRM intra cavity loss can be inferred from the power recycling factor. This can be done since the power in, the power out and mirror reflectivities of the PRM are known. These parameters along with power recycling factor are used in the model presented in chapter 4 to calculates the intra cavity loss.

$$F_{90\%} \Longrightarrow \text{Loss}_{intra} = 8 \pm 0.8\% \tag{6.4}$$

The reason for the high intra cavity loss is unclear. The measured fringe visibility for the Michelson is very high which ensures that the loss is not only in one arm of the Michelson. Thus the loss is either in the power recycling mirror or symmetric loss in the Michelson, or a combination of both. The location is unimportant for the PRM, but it is important for the simple Michelson. We consider two extreme cases to give the upper and lower bound on loss to squeezed light for the simple Michelson;

· Case 1: The loss is in the Michelson.

· Case 2: The loss is in the power recycling mirror.

Both these cases are modelled for comparison with the results.

6.2.3 Injection optics loss

The injection of the squeezed light into the interferometer is performed using a Faraday isolator. This method maintains the standard gravitational wave detector configuration, however a large loss of squeezed light was encountered. The loss was measured by increasing the squeezed light DC power and comparing it before and after the double pass of the isolator. We measured a double pass loss of,

$$\text{Loss}_{inj} = 15\% \tag{6.5}$$

Although this is less than the manufacturer's specified single pass loss of 0.5dB (10%) it was a substantial loss of squeezed light. The 15% loss was reduced to as low as 5% using a different isolator (OFR), however this came at the expense of poor isolation. Poor isolation presented problems with the OPA locking, as some of the power in the PRM was transmitted towards the OPA. This created an uncontrolled low finesse cavity, with the PRM acting as one mirror and the OPA acting as the other mirror. The OPA lock was effected creating unpredictable experimental behavior.

The cause of poor isolator performance is thought to be an imperfect Faraday rotator. If the magnetic field in the rotator is partially inhomogeneous, the rotation of the polarization state is not exactly 45^0 single pass. After double pass not all of the vertically polarized light is converted to horizontally polarized state. Consequently the isolation was poor and some of the light from the PRM was transmitted towards the OPA. The isolation was improved by rotating the polarizing beam splitter cube slightly off its usual 45^0. This ejected the incorrectly polarized light from the system and increased the loss[6].

With a Faraday isolator correctly setup it is expected that the double pass loss of the isolator could potentially be as low as 1%, given by transmission loss of the crystal (such as terbium gallium garnet with absorption of 0.55% cm^{-1}).

6.3 Power recycled Michelson with squeezed light

In this section the main results of the experiment are presented. The noise out of the PRM with squeezed light is compared to the squeezed light in, and the interaction of squeezing with power recycling is demonstrated.

6.3.1 Noise out of the PRM

The measured noise on the carrier field noise at the output of the PRM with a 90% power mirror are shown in Figure 6.5. Trace (a) shows the noise on the carrier when squeezed light was injected into the PRM with the phase scanned. Trace (b) shows the SNL, at $\approx -84.6 \pm 0.2\text{dBm}$, which was flat across 5-6MHz. Trace (c) shows the carrier noise when the squeezed light is injected and the phase is locked to the minimum projection of noise. The noise was 86.7 ± 0.2dB, which was 2.3 ± 0.2dB below the SNL. Trace (d), the straight line, is the modelled prediction of the carrier noise given the losses inferred in the previous section.

[6]The uncontrolled cavity could be used for good rather than evil. If the effect of the uncontrolled cavity was seen, then the alignment of the squeezed light to the OPA was very good. The PBS was then rotated slightly and the isolation was improved.

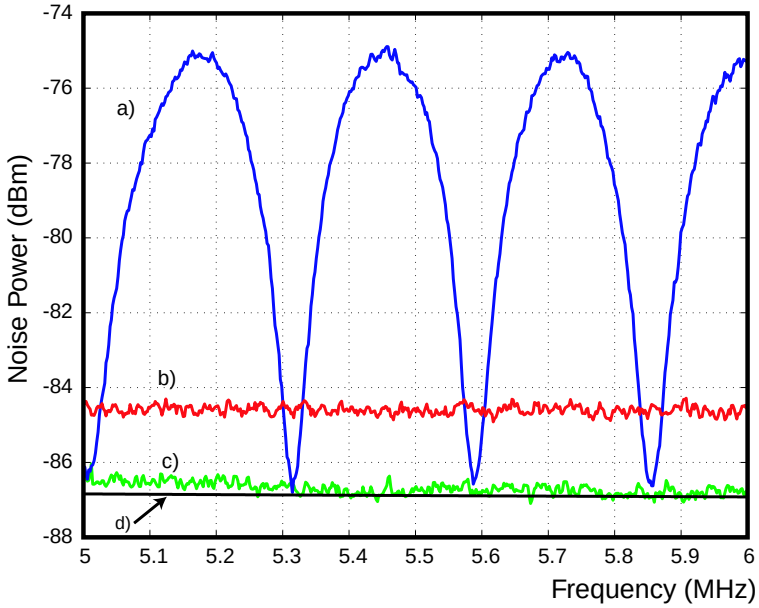

Figure 6.5: a) The noise power on the carrier light at the output of the PRM with 90% reflectivity power mirror from 5-6 MHz. This is shown with a)Scanned squeezed light injected, b)Shot noise and c)Locked squeezed light injected. d) The modelled prediction of the carrier noise. (straight line). The electronic noise floor is approximately flat across the frequency scan lying at -95 dBm. RBW = 100kHz, VBW = 30 Hz

The noise on the carrier light in figure 6.5 (c) can be compared with the squeezed light before it entered the PRM, shown in figure 6.2 (a). Before squeezed light entered the PRM it was measured to be 3.3 ± 0.2dB below the SNL and after the PRM it was measured to be 2.3 ± 0.2dB. Thus a reduction of squeezing by approximately 20% was measured. This reduction is consistent with the prediction of the model which is 2.46 ± 0.2dB.

6.3.2 Characterization of the system

The PRM with squeezed light is characterized with a signal at 5.46MHz. Figure 6.6 trace (a) shows the results for a simple Michelson. This noise floor is at the SNL. When squeezing is introduced, trace (b), we find a noise suppression of 1.8 $\pm$0.2 dB below the SNL. Traces (c) and (d) show the response of the 90% PRM with and without the squeezed input. The power recycling factor is $\approx$ 9.5. The noise floor of trace (d) is 2.3 $\pm$ 0.2 dB lower than SNL. The predicted improvement that is shown in figure 4.5 of the squeezing performance with power recycling is evident in the different noise floors of traces (b) and (d). The amount of squeezing before injection is shown in the figure 6.2 a). It can be seen that a reduction of 15-20% was measured after interaction with the 90% PRM. The measured and predicted values for noise reduction below the SNL in the 90% PRM are,

$$N_{PRM} = 2.3 \pm 0.2\text{dB (Measured)} \quad \leftrightarrow \quad 2.4\text{dB (Modelled)} \tag{6.6}$$

This measured result corresponds to the model's predictions within the experimental error. For the simple Michelson the measured and predicted values for noise reduction

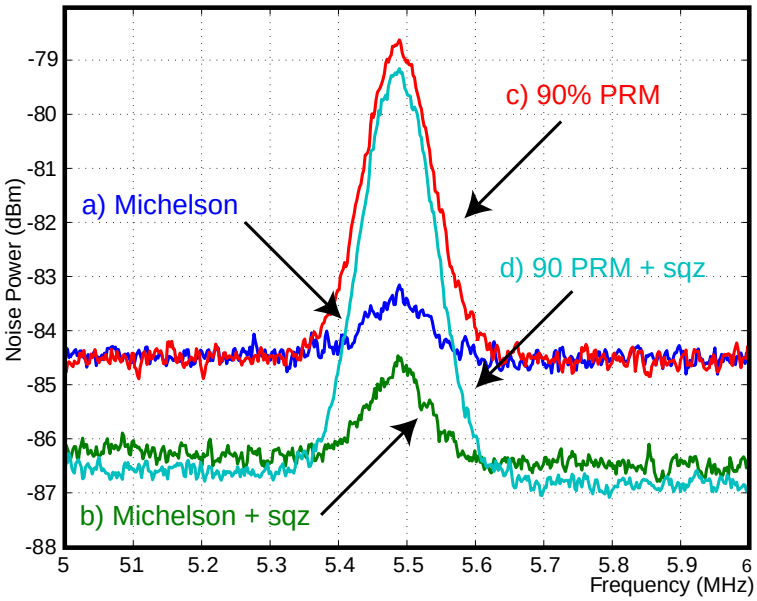

Figure 6.6: Results of noise floor and a signal for a) a simple Michelson, b) a simple Michelson with locked squeezing, c) a power recycling Michelson and d) a power recycled Michelson with locked squeezing. Electronic noise lies at -93.5dBm, The signal is at 5.46 MHz . RBW = 100 kHz, VBW = 30 Hz

below the SNL are,

$$N_{SM} = 1.8 \pm 0.2\text{dB (Measured)} \quad \leftrightarrow \quad 1.7\text{dB (Modelled case1)} \tag{6.7}$$

$$\leftrightarrow \quad 2.1\text{dB (Modelled case2)} \tag{6.8}$$

These two cases of the model represent the extremes of the loss distribution intra cavity, hence the experimental result should have fallen between the their values, as it did. The first case of the modelled predictions, that is the loss is located in the Michelson, was very close to the experimental results. It is thought more likely that the loss would be in the Michelson than the power mirror, as in the Michelson their are five surfaces that the light is incident on and loss could occur, whereas the power mirror only has one. It could also be a combination of Michelson and power mirror loss.

6.3.3 PRM with squeezed light locking performance

Good locking stability in gravitational wave detectors is vital for their continuous operation. In our experiment we wish to demonstrate that our control scheme can lock the entire system. The locking stability of our system is different to that achievable in the vacuum conditions of a long baseline gravitational wave detector. The difference is principally attributed to thermal fluctuations in the atmospheric environment in the laboratory. Figure 6.7 shows the locked PRM with locked squeezed light over a 15 minute period. It shows a trace of the carrier noise and shot noise at 5.5MHz. The limit to the locking stability is expected to be from the limited range of the PZTs and the effect of

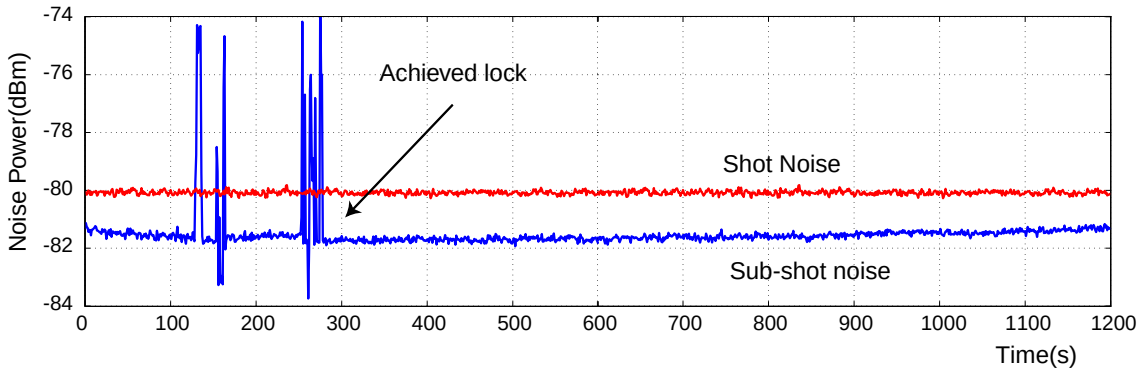

Figure 6.7: Carrier noise at the output of the locked PRM with squeezed light for over 15 minutes. Traces taken at 5.5MHz, zero frequency span. RBW =330kHz, VBW = 30HZ

temperature change.

The trace of the carrier noise shows a slight reduction of squeezing over time. The reduction could be attributed to a possible reduction of squeezed light out of the OPA. On another occasion it has been shown that the squeezed light could be locked without reduction for over one hour [27].

6.3.4 Comparison of different power mirror reflectivities

To further investigate the interaction of squeezed light with power recycling, a data run was taken using two different power mirror reflectivities. Figure 6.8 traces (b) and (c) show the carrier noise below the shot noise level for the 90% and 97% power mirror reflectivities, respectively. The squeezed light was not measured before these results were taken, the model assumes the regularly seen 3dB of squeezing. The power recycling factors for the 90% and 97% power mirror reflectivities were obtained from the figure 6.8 (a). The power recycling factors and inferred intra cavity losses are,

$$F_{90\%} = 7.1 \pm 1.0\text{dB} \implies \text{Loss}_{intra90\%} = 11 \pm 1.1\% \tag{6.9}$$

$$F_{97\%} = 9.9 \pm 1.0\text{dB} \implies \text{Loss}_{intra97\%} = 6 \pm 0.6\% \tag{6.10}$$

These results are taken with a Michelson fringe visibility of 99%. The straight lines in figure 6.8 traces (b) and (c) show the modelled predictions using these inferred losses. The modelled traces agree with the results within the experimental errors.

Their was a discrepancy between the power recycling factors for the 90% power mirror in the two data runs of the experiment (first data run $F_{90\%} = 9.5$, second data run $F_{90\%} = 7.1$). This may have been caused by extra loss due to poor alignment after changing the power mirror from the 90% reflectivity to the 97% reflectivity.

The alignment procedure for the 97%/90% PRM was as follows: the 97% power mirror was aligned with the Michelson by varying both the power mirror and Michelson arms tilt. The squeezed light is then aligned and optimized for the 97% PRM, and data was taken. The 97% mirror was then replaced by the 90% PRM. Since the squeezed light was already aligned into the Michelson, the alignment was not changed. The 90% power

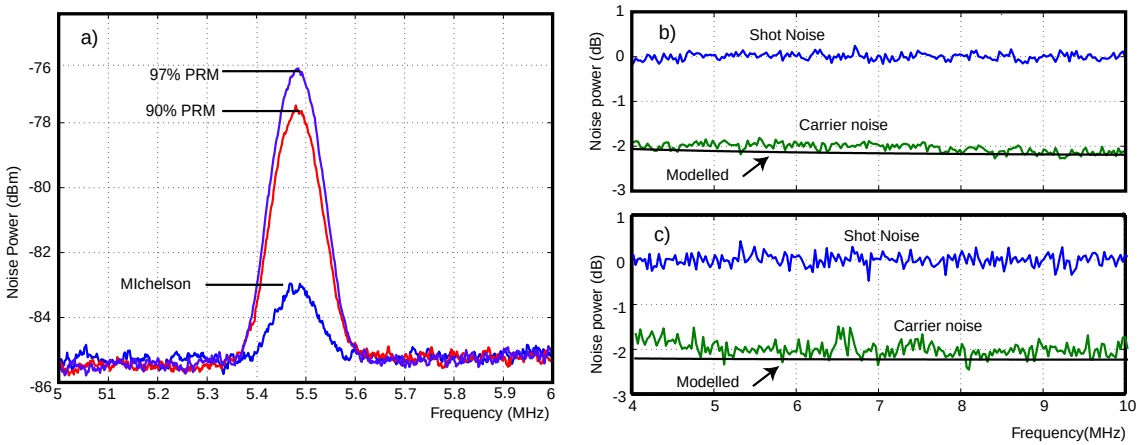

Figure 6.8: a)The signal measured at 5.46MHz by the Michelson and the 90% and 97% reflectivity PRM's. b) The carrier noise spectrum with squeezing measured with the 90% reflectivity PRM and the models prediction (straight line). c) The carrier noise spectrum with squeezing measured with the 97% reflectivity PRM and the model prediction (straight line)

mirror was the aligned to the Michelson. This method was much more difficult to align as there was only one degree of freedom to control.

It was hoped that their would be some distinction in the results between the 90% reflectivity and 97% reflectivity PRMs, however both the model and results are similar for both cases. To obtain a better comparison it would be ideal to operated at lower frequency, closer to the PRM cavity linewidths. Near the cavity linewidths the PRM's complex reflectivities have quite different responses, and it is thought these differences could be measured. These low frequencies could not be accessed since the carrier light is not SNL until ∼4MHz.

6.4 Summary of results

The results presented here show the first experimental demonstration of an interferometric gravitational wave detector configuration that operated below the shot noise limit. Squeezed light was injected into the PRM and a reduction of 2.3dB below the shot noise limit was obtained. The interaction of the squeezed light with the Michelson, with and without power recycling has been analyzed. The improvement when power recycling was introduced has been demonstrated and confirms the model's predictions. Conclusive evidence of the effect on the interaction of squeezed light with the PRM using different power recycling mirrors was unable to be obtained. The control of the PRM was shown to be compatible with squeezed light since the entire system was stably locked for over 15 minutes. The system lock is thought to be limited only by the PZT range and the thermal stability of the laboratory. Comparison of the predictions of the model derived in chapter 4 with the experimental results an excellent level of agreement.

Chapter 7

Conclusion and further work

This thesis has introduced gravitational wave detection, the theory of quantum noise, and squeezed light. The method of linearized operators was presented to simplify quantum noise calculations in the derivation of the properties of a power recycled Michelson interferometer with squeezed light. The optical layout and control techniques have been presented. The configuration, control scheme, injection of the squeezed light and signal readout demonstrated in this experiment are all compatible with current gravitational wave detectors.

The results presented are the first experimental demonstration of an interferometric gravitational wave detector configuration operated below the shot noise limit. The noise was measured to be 2.3dB below the shot noise limit. The interaction between the squeezed light and the Michelson, with and without power recycling was analyzed, and it was determined that use of power recycling improves the amount of shot noise reduction. The predictions by the model derived with linearized operators show excellent agreement with the experimental results. The entire system locked stably for over 15 minutes. The locking stability is thought to be limited only by the PZT range and the thermal stability of the laboratory.

7.1 Further Work

It is expected that this research is the first of many experiments using squeezed light in gravitational wave detector configurations, with the view to ultimately applying squeezed light to long base line interferometric detectors. One such experiment is at an early stage of planning, involves building up a similar experiment in collaboration with Massachusetts Institute of Technology.

Since second generation detectors are expected to employ resonant sideband extraction, the investigation of the interaction of squeezed light with this configuration is imperative. Also, the second generation of detectors are expected to have high enough optical power to reach the radiation pressure noise regime. Thus detectors would be limited by radiation pressure noise at low frequencies of 10Hz-100Hz and shot noise above 100Hz. Squeezed light could be used in such a interferometer, with the correct preparation to reduce radiation pressure noise at low frequencies and shot noise at high frequencies. At $\sim$100Hz, where the two noise sources are equal called the standard quantum limit, squeezed light can be used to reach sensitivities below this point[4].

Bibliography

[1] A. Einstein, Preuss. Akad. Wiss. Berlin , 688 (1916).

[2] A. Einstein, Ann. Phys. Lpz **49**, 769 (1916).

[3] N. A. Robertson, *Laser interferometric gravitational wave detectors*, Class. Quantum Grav. **17**, R19 (2000).

[4] D. F. Walls and G. J. Milburn, *Quantum Optics*, Springer-Verlag, Berlin, 1 edition, 1994.

[5] C. M. Caves, *Quantum-mechanical noise in an interferometer*, Phys. Rev. D. **23**, 1693 (1981).

[6] J. Gea-Banacloche and G. Leuchs, *Squeezed states for interferometric gravitational-wave detectors*, Journal of Modern Optics **34**, 93 (1987).

[7] V. J. Chickamane, S. V. Dhurandhar, T. C. Ralph, M. Gray, H-A. Bachor, and D. E. McClelland, *Squeezed light in a frontal phase-modulated signal-recycled interferometer*, Phys. Rev. A **57**, 3898 (1998).

[8] H. J. Kimble, Y. Levin, A. B. Matsko, K. S. Thorne, and S. P. Vyatchanin, *Conversion of conventional gravitational-wave interferometers into quantum nondemolition interferometers by modifying their input and/or output optics*, Phys. Rev. D **65**, 31 (2002).

[9] C. W. Misner, K. S. Thorne, and J. L. Wheeler, *Gravitation*, Freeman, San Francisco, 1973.

[10] P. R. Saulson, *Fundamentals of interferometric gravitational wave detectors*, World Scientific, Singapore, 1 edition, 1994.

[11] J. H. Taylor and J. M. Weisberg, *A new test of general relativity: gravitational radiation and the binary pulsar PSR 1913+16*, Astrophys. J. (Letters) **253**, 908 (1982).

[12] R. A. Hulse and J. H. Taylor, *Discovery of a pulsar in a binary system*, Astrophys. J. (Letters) **195**, L51 (1975).

[13] B. J. Meers, *Recycling in laser-interferometric gravitational-wave detectors*, Phys. Rev. D **38**, 2317 (1988).

[14] B. E. A Saleh and M. C. Teich, *Fundamentals of Photonics*, Wiley Interscience, New York, 1973.

[15] A. Abramovici, W. E. Althouse, R. W. P. Drever, Y. Gursel, S. Kawamura, F. J. Raab, D. Shoemaker, L. Sievers, R. E. Spero, K. S. Thorne, R. E. Vogt, R. Weiss, S. E. Whitcomb, and M. E. Zucker, *LIGO: the Laser Interferometer Gravitational-Wave Observatory*, Science **256**, 325 (1992).

[16] A. Brillet et al., Virgo proposal to CNRS and INFN, unpublished, 1989.

[17] M. Ando, K. Tsubono, and the TAMA collaboration, *TAMA Project: design and current status*, Gravitational Waves: Third Edoardo Amaldi Conference, Pasadena. ed S. Meshkov , 128 (2000).

[18] H. Lück, P. Aufmuth, O. S. Brozek, K. Danzmann, A. Freise, S. Goßler, A. Grado, H. Grote, K. Mossavi, V. Quetschke, B. Willke, K. Kawabe, A. Rüdiger, R. Schilling, W. Winkler, C. Zhao, K. A. Strain, C. Cagnoli, M. Casey, J. Hough, M. Husman, P. McNamara, G. P. Newton, M. V. Plissi, N. A. Robertson, S. Rowan, D. I. Robertson, K. D. Skeldon, C. I. Torrie, H. Ward, B. F. Schutz, I. Taylor, and B. S. Sathyprakash, *The status of GEO600*, Gravitational Waves: Third Edoardo Amaldi Conference, Pasadena. ed S. Meshkov , 119 (2000).

[19] E. Gustafson, D. Shoemaker, K. Strain, and R.Weiss, *LSC White Paper on Detector Research and Development*, LIGO T990080-00-D (1999).

[20] D. A. Shaddock, M. B. Gray, C. Mow-Lowry, and D. E. Mclelland, *A power recycled Michelson Interferometer with resonant sideband extraction*, To be published .

[21] R. E. Slusher, L. W. Hollberg, B. Yurke, J. C. Mertz, and J. F. Valley, *Observation of Squeezed States Generated by Four-Wave Mixing in an Optical Cavity*, Phys. Rev. Lett. **55**, 2409 (1985).

[22] P. K. Lam, *Applications of quantum electro-optic control and squeezed light*, PhD thesis, Physics Department, Australian National University, Canberra, Australia, 1998.

[23] Min Xiao, Ling-Au Wu, and H. J. Kimble, *Precision Measurement beyond the Shot-Noise Limit*, Phys. Rev. Lett **59**, 278 (1987).

[24] P. Grangier, R. E. Slusher, B. Yurke, and A. LaPorta, *Squeezed-Light-Enhanced Polarization Interferometer*, Phys. Rev. Lett **59**, 2153 (1987).

[25] H. Haken, *"Laser theory", in Encyclopedia of Physics, Vol. XXV/2c, Light and Matter 1c*, Springer-Verlag, Berlin, 1 edition, 1970.

[26] B. Yurke, *Use of cavities in squeezed state generation*, Phys. Rev. A **20**, 408 (1984).

[27] B. C. Buchler, *Electro-optic control of quantum measurements*, PhD thesis, Physics Department, Australian National University, Canberra, Australia, 2001.

[28] R. W. P. Drever, J. L. Hall, F. V. Kowalski, J. Hough, G. M. Ford, A. J. Munley, and H. Ward, *Laser phase and frequency stabilization using an optical resonator*, Appl. Phys. B , 31 (1983).

[29] L. Schnupp, Conference presentation, in *European collaboration Meeting on Interferometric Detection of Gravitational Waves*, 1988.

[30] B. C. Buchler, Feedback Control of Laser Intensity Noise, Master's thesis, Physics Department, Australian National University, Canberra, Australia, 1996.

[31] D. A. Shaddock, M. B. Gray, and D. E. Mclelland, *Frequency locking a laser to an optical cavity by use of spatial mode interference*, Opt. Lett. **24**, 1499 (1999).

[32] M. B. Gray, D. A. Shaddock, C. C. Harb, and H.-A. Bachor, *Photodetector designs for low-noise, broadband, and high power applcations*, Rev. Sci. Instrum. **69**, 3755 (1998).

[33] D. A. Shaddock, *Advanced interferometry for gravitational wave detection*, PhD thesis, Physics Department, Australian National University, Canberra, Australia, 2000.

Appendix A

Derivation of Transfer functions

Derivation of the Power Recycled Michelson with a Squeezed Input at the Dark Port of the Michelson

A schematic of the experimental setup for the PRM with squeezing is shown in figure 4.2 (a). A equivalent model is shown in figure 4.2 (b). This representation uses a Fabry Perot ring cavity. The three mirrors represent: The power recycling mirror with reflectivity and transmisson, r_p,t_p, the Michelson interferometer with r_m,t_m and losses in the cavity with, r_l,t_l. The loss mirror transmission, t_l is equal to the total round trip loss in the cavity. The fields in the model are represented in the frequency domain using the linearized operators. The three fields that couple to the output of the interferometer are; the carrier, the squeezing and the vacuum fluctuations,

$$\hat{a}_{in} \tag{A.1}$$

$$\hat{a}_{s} \tag{A.2}$$

$$\hat{a}_{v} \tag{A.3}$$

The fields all enter from a different port. Explicit frequency dependence is not shown here, as all of the fields are frequency dependent it is implied. The field circulating inside the cavity in steady state, $\hat{a}_{circ}$ is defined to be the sum of all the fields multiplied by the appropriate transmission into the cavity located just after the power mirror, r_p. Thus it is a sum of; $\hat{a}_{in}$ multiplied by the transmission of the power mirror, t_p. $\hat{a}_s$ multiplied by the reflectivity of the Michelson, t_m, and the reflection off the loss mirror, r_l and the power mirror, r_p and it receives a phase shift during cavity round trip of, ϕ_v. $\hat{a}_v$ multiplied by the transmission of the loss mirror t_l and the reflection off the power mirror. Plus the circulating field already in the cavity advanced by a round trip.

$$\hat{a}_{circ} = it_p\hat{a}_{in} + it_m r_l r_p \mathrm{e}^{iphi_v}\hat{a}_s + it_l r_p \mathrm{e}^{i\phi_v} + r_m r_l r_p \mathrm{e}^{2i\phi_v}\hat{a}_{circ} \tag{A.4}$$

which can be solved for $\hat{a}_{circ}$,

$$\hat{a}_{circ} = \frac{it_p\hat{a}_{in} + it_m r_l r_p \mathrm{e}^{i\phi_v}\hat{a}_s + it_l r_p \mathrm{e}^{i\phi_v}}{1 - r_m r_l r_p \mathrm{e}^{2i\phi_v}} \tag{A.5}$$

Now the field at the output, $\hat{a}_{out}$ can be written down.

$$\hat{a}_{out} = it_m e^{i\phi}\hat{a}_{circ} + r_m\hat{a}_s \quad (A.6)$$

$$= \frac{-t_m t_p e^{i\phi}\hat{a}_{in} - t_m^2 r_l r_p e^{2i\phi_v}\hat{a}_s + -t_m t_l r_p e^{2i\phi_v}}{1 - r_m r_l r_p e^{2i\phi_v}} + r_m\hat{a}_s \quad (A.7)$$

now this can be separated into components of each field. For the input field, $\hat{a}_{in}$,

$$\hat{a}_{out} = \frac{-t_m t_p e^{i\phi}\hat{a}_{in}}{1 - r_m r_l r_p e^{2i\phi_v}} \quad (A.8)$$

thus the transfer function of the field $\hat{a}_{in}$ is,

$$T_\alpha = \hat{a}_{out}/\hat{a}_{in} \quad (A.9)$$

$$= -\frac{t_p t_m e^{i\phi_v}}{1 - r_p r_m r_l e^{i2\phi_v}} \quad (A.10)$$

Similarly for $\hat{a}_s$,

$$\hat{a}_{out} = \frac{-t_m^2 r_l r_p e^{2i\phi_v}\hat{a}_s}{1 - r_m r_l r_p e^{2i\phi_v}} + r_m\hat{a}_s \quad (A.11)$$

$$= \frac{r_m - r_p r_l e^{i2\phi_v}}{1 - r_p r_m r_l e^{i2\phi_v}}\hat{a}_s \quad (A.12)$$

which gives the transfer function for $\hat{a}_s$,

$$T_{a_s} = \hat{a}_{out}/\hat{a}_s \quad (A.13)$$

$$= \frac{r_m - r_p r_l e^{i2\phi_v}}{1 - r_p r_m r_l e^{i2\phi_v}} \quad (A.14)$$

and for $\hat{a}_v$,

$$\hat{a}_{out} = \frac{-t_m t_l r_p e^{2i\phi_v}}{1 - r_m r_l r_p e^{2i\phi_v}} \quad (A.15)$$

and the transfer function is,

$$T_{\delta a_v} = \hat{a}_{out}/\hat{a}_s \quad (A.16)$$

$$= -\frac{t_m t_l r_p e^{i\phi_v}}{1 - r_p r_m r_l e^{i2\phi_v}} \quad (A.17)$$

Explicit frequency dependence has not been stated in this derivation, it is contained in the phase shift ϕ_v.

Model MatLab code

B.1 Code for PRM with squeezed light

```
% This file is used to simulate squeezng in a power recycled
% michelson. It is used to plot squeezing measured at the output
% detector as a function of frequency
% It calls the transfer functions from ringTFfreq.m

clear all;

global tbs rbs rp tp tm rml rms r3 t3 x0 x y z a_in freq P_out G
Aw_sq f_sq

%%%%%%%%%%%%%%%%% Interferometer parameters %%%%%%%%%%%%%%%%%%

P_in = 20;                      % power into michelson (mW)
a_in = sqrt(P_in);              % amplitude coming into michelson
c = 3e8;                        % speed of light
f_sq = linspace(4e6,10e6,1001); % frequency of the squeezing
w_sq = 2*pi*f_sq;

Rp=0.0;                 % Power recycling mirror reflectivity
Ap=0.0;                 % Power recycling mirror loss

R3 = 1;                 % 3rd mirror used to simulate loss
A3 = 0;                 % 3rd mirror loss.

Loss = .15;
A = (1-Loss);           % Simulates loss in the rotator

Rbs=0.5;                % Main beamsplitter reflectivity
Abs=0.0;                % Main beamsplitter loss

rp=sqrt(Rp);            % Power  mirror amplitude reflectivity
tp=sqrt(1-Ap-Rp);       % Power  mirror amplitude transmissivity
```

```
r3=sqrt(R3);            % 3rd mirror amplitude reflectivity
t3=sqrt(1-A3-R3);       % 3rd mirror amplitude transmissivity

rbs=sqrt(Rbs);          % beamsplitter amplitude reflectivity
tbs=sqrt(1-Rbs-Abs);    % beamsplitter amplitude transmissivity

%%%%%%%%%%%%%%%%%%%%%%%% Interferometer lengths %%%%%%%%%%%%%%%%

Lp=1;                       % Distance from main beamsplitter to PRM
Lm=0;                       % Average distance from main beamsplitter
                            % to Michelson mirrors
dL=0;                       % Michelson arm length mismatch

%%%%%%%%%%%%%%%%%%%%%%%% Interferometer phases %%%%%%%%%%%%%%%%

phi_p0=0; phi_m0=0;
phi_d0=0.27;    % offset of the michelson from a dark fringe;


%%%%%%%%%%%%%%%%%%%%%%%%5% Phases of variences %%%%%%%%%%%%%%%%%%%%

phi_x0x = 0;        %phase of laser fluctuations relative to the carrier
phi_x0y = 0;        %phase of squeezing fluctuations relative to carrier
phi_x0z = 0;        %phase of vaccum fluctuations relative to carrier

%%%%%%%%%%%%%%%%%%%%%%%%%%%%%% Carrier Field %%%%%%%%%%%%%%%%%%%%%

w=0;                                % frequency offset from carrier
phi_p=w*Lp/c+phi_p0;            % PRC single pass phase
phi_m=w*Lm/c+phi_m0;            % Ave Mich single pass phase
phi_d=w*dL/c+phi_d0;            % Diff Mich single pass phase

%%%%%%%%%%%%%%%%%%%%%%%%%%%%%% Squeeze Field %%%%%%%%%%%%%%%%%%%%%

phi_sqm=phi_m+(w_sq)*(Lm)/c;    % Phase shift SQZ receives in michelson
phi_sqp=phi_p+(w_sq)*(Lp)/c;    % Phase shift SQZ receives in power cavity

%%%%%%%%%%%%%%%%%%%%%%%%%%%%%%%%%%%%%%%% Call the varience from ringTFfrq %%%%%

[V] =
ringTFfreq(phi_p,phi_m,phi_d,phi_x0x,phi_x0y,phi_x0z,phi_sqm,phi_sqp)
;

minsq = min(10*log10(V)) maxsq = max(10*log10(V))

%$%%%%%%%%%%%%%%%%%%%%%%%%%%%%%%%%%%%%%%%%%%%%%%%% Plots %%%%%%%%%%%%%%%%%%%%%%%%%%%%

figure(1) subplot(3,1,1) plot(f_sq,10*log10(V))
```

```
title('Squeezing vs freq.(flat 3dB input)(90% PRM and simple mich)')
axis([4e6 10e6 -3 1]) grid on; hold on;
```

B.2 transfer functions for PRM with squeezed light

```
%transfer functions file = ringTFfreq.m

function [V] =
ringTFfreq(phi_p,phi_m,phi_d,phi_x0x,phi_x0y,phi_x0z,phi_sqm,phi_sqp)

% this is used to define transfer functions for  michelson ect

global tbs rbs rp tp tm rml rms r3 t3 x0 x y z a_in phi_x0z freq
P_out G A w_sq f_sq


%%%% Phases and variences of fluctuations %%%%

dXap = 1/sqrt(1);              % Amplitude fluctiations on laser
dXam = 1/dXap;                 % Phase fluctions on laser
dXsp = 1/sqrt(A*(1/0.5));      % Amplitude fluctiations of squeezing
dXsm = 1/dXsp;                 % Phase fluctions of squeezing
dXlp = 1/sqrt(1);              % Amplitude fluctiations of vaccum
dXlm = 1/dXlp;                 % Phase fluctions of vaccum

%%%% Define Michelson ref/trans for the carrier %%%%

rml = (tbs^2.*(exp(i*2*phi_d))+ rbs^2.*(exp(-i*2*phi_d)))
        .*exp(i*2*(phi_m)) ;   % [Eref/Ein]
rms = (tbs^2.*(exp(-i*2*phi_d)) + rbs^2.*(exp(i*2*phi_d)))
        .*exp(i*2*(phi_m));   % [Ed/Es]
tm  =  i*rbs.*tbs.*(exp(i*2*phi_d)-exp(-i*2*phi_d))
        .*exp(i.*2.*(phi_m));        % [Eref/Es]

%%%% Define Michelson ref/trans for squeezing %%%%

rml_sq = (tbs^2.*(exp(i*2*phi_d))+ rbs^2.*(exp(-i*2*phi_d)))
           .*exp(i*2*(phi_sqm)) ;% [Eref/Ein]
rms_sq = (tbs^2.*(exp(-i*2*phi_d)) + rbs^2.*(exp(i*2*phi_d)))
           .*exp(i*2*(phi_sqm));% [Ed/Es]
tm_sq =  i*rbs.*tbs.*(exp(i*2*phi_d)-exp(-i*2*phi_d))
           .*exp(i.*2.*(phi_sqm));         % [Eref/Es]

%%%% Cavity Transfer Functions %%%%%

x0 = -tp.*tm.*exp(i.*(phi_p+phi_m))./
```

```
            (1 - rp.*rml.*r3.*exp(i*2.*(phi_p+phi_m)));
            % x0 is the coefficient in transfer function for the carrier

d = (1 - rp.*rml_sq.*r3.*exp(i*2.*(phi_sqp+phi_sqm)));
                % denominator for each variable, x, y, z.
x = -tp.*tm_sq.*exp(i.*(phi_sqp+phi_sqm))./d;
                %transfer function for the noise on the laser
y = (rms_sq - rp.*rml_sq.*rms_sq.*r3.*exp(i*2.*(phi_sqp+phi_sqm))
        - tm_sq.^2.*rp.*r3.*exp(i*2.*(phi_sqp+phi_sqm))).*d;
        %transfer function for squeezing (function of frequency)
z = -tm_sq.*t3.*rp.*exp(i*2.*(phi_sqp+phi_sqm))./d  ;
         %transfer function for the vaccum noise due to losses

%%%% Squeezing out as a function of frequency %%%%

sq_out = (rms_sq - r3*rp.*exp(i*(2*phi_sqm+phi_sqp)).*(tm_sq.^2 +
rml_sq.*rms_sq))./(1-rml_sq.*r3*rp.*exp(i*(2*phi_sqm+phi_sqp)));


%%%% Normalising factor  %%%%

T = a_in^2*(abs(conj(x0).*x).^2+abs(conj(x0).*y)
        .^2+abs(conj(x0).*z).^2);  %normalising factor

Cx = a_in^2*abs(conj(x0.*x)).^2./T;

Cy = a_in^2*abs(conj(x0.*y)).^2./T;

Cz = a_in^2*abs(conj(x0.*z)).^2./T;

%%%% Signal at output and Varience %%%%

V = Cx.*(dXap.^2.*cos(phi_x0x).^2+dXam.^2.*sin(phi_x0x).^2) + ...
    Cy.*(dXsp.^2.*cos(phi_x0y).^2+dXsm.^2.*sin(phi_x0y).^2) + ...
    Cz.*(dXlp.^2.*cos(phi_x0z).^2+dXlm.^2.*sin(phi_x0z).^2) ;
    % Normalised Varience at dark port
```

Appendix C

MatLab code for gain estimates

C.1 Main file

```
% This m-file model the error signal response of the power-recyled
% Michelson intereferometer with a bright squeezed input at the dark
% fringe. It is intended for control purposes only.
%
% K. McKenzie 8/2001.

global tbs rbs rp tp tm rml rms FWHM

PLO = 20;                   % Local oscillator power [mW]
PS = 0;                     % Squeezed input power [mW]

c = 3e8;                    % speed of light [m/s]
fm = 75.9e6;                % modulation frequency [Hz]
delta = 0.1;                % modulation depth [radians]
phi_demod = 0*pi/180;       % demodulation phase [radians]

%%%% Interferometer parameters %%%%

Rp=0.9;             % Power recycling mirror reflectivity
Ap=0.005;           % Power recycling mirror loss

Rbs=0.5;            % Main beamsplitter reflectivity
Abs=0.0;            % Main beamsplitter loss

rp=sqrt(Rp);        % Power recycling mirror amplitude reflectivity
tp=sqrt(1-Ap-Rp);   % Power recycling mirror amplitude transmissivity

rbs=sqrt(Rbs);      % Main beamsplitter amplitude reflectivity
tbs=sqrt(1-Rbs-Abs);% Main beamsplitter amplitude transmissivity

%%%% Interferometer lengths %%%%

Lp=0.6;             % Distance from main beamsplitter to PRM
Lm=0.4;             % Distance from main beamsplitter to Michelson
```

```
dL=0.;              % Michelson arm length mismatch

%%%% Interferometer phases %%%%

start=-100;         % start point of scanning phase [degrees]
stop=-start;        % stop point of scanning phase [degrees]
points=10000;       % number of plotting points

phi_offset = linspace(start,stop,points)*pi/180;% offset phase [radians]

phi_p0=0; phi_m0=0;
phi_d0= phi_offset;%-1.926*pi/180;%for 1/2% loss %-1.873*pi/180; %
phi_s0=0;

%%%% Carrier Field %%%%

w=0;                            % frequency offset from carrier

phi_p=w*Lp/c+phi_p0;            % PRC single pass phase
phi_m=w*Lm/c+phi_m0;            % Ave Mich single pass phase
phi_d=w*dL/c+phi_d0;            % Diff Mich single pass phase
phi_s=phi_s0;                   % signal recycling phase

Ein=sqrt(PLO); Es=sqrt(PS)*exp(i*phi_s);

[Ed,Er]=PRMtf(phi_p,phi_m,phi_d,Ein,Es);

%%%% Upper sideband field %%%%

w=2*pi*fm;

phi_p=w*Lp/c+phi_p0;            % PRC single pass phase
phi_m=w*Lm/c+phi_m0;            % Ave Mich single pass phase
phi_d=w*dL/c+phi_d0;            % Diff Mich single pass phase
phi_s=phi_s0;                   % signal recycling phase

Ein=delta/2*sqrt(PLO); Es=0;

[Ed1,Er1]=PRMtf(phi_p,phi_m,phi_d,Ein,Es);

%%%% Lower sideband field %%%%

w=-2*pi*fm;

phi_p=w*Lp/c+phi_p0;            % PRC single pass phase
phi_m=w*Lm/c+phi_m0;            % Ave Mich single pass phase
phi_d=w*dL/c+phi_d0;            % Diff Mich single pass phase
phi_s=phi_s0;                   % signal recycling phase
```

```
Ein=delta/2*sqrt(PLO); Es=0;

[Ed_1,Er_1]=PRMtf(phi_p,phi_m,phi_d,Ein,Es);

%%%% Error signals %%%%

Dr=(conj(Er).*Er1-Er.*conj(Er_1))*exp(i*phi_demod);
        % Reflected field discriminant
Dd=(conj(Ed).*Ed1-Ed.*conj(Ed_1))*exp(i*phi_demod);
        % Transmitted field discriminant

Ir=imag(Dr); Qr=real(Dr); Id=imag(Dd); Qd=real(Dd);

Fdc = abs(Ed).^2-PLO*0.15;

%%%% Calculate Slopes of error signals %%%%

Fdcslope = (Fdc(points/2+1)-Fdc(points/2-1))/(-4*start/points)
Irslope = (Ir(points/2+1)-Ir(points/2-1))/(-4*start/points)

%%%% Control matrix %%%%
C = [ 2.2690 -0.0350
     -0.6501 -2.9206 ]

Ci = inv (C)

%%%%%%%%%%%%

%%%% Plots %%%%
figure(1) subplot(3,1,1) plot(phi_offset*180/pi,abs(Ed).^2)
title('Power at dark port') subplot(3,1,2)
plot(phi_offset*180/pi,abs(Er).^2) title('Reflected Power')
subplot(3,1,3) plot(phi_offset*180/pi,Fdc) title('Offset locking
error signal')

% figure(3)
% plot(phi_offset*180/pi,FWHM)

figure(2)

subplot(2,2,1) plot(phi_offset*180/pi,abs(Er).^2) title('Reflected
Power (mW)') subplot(2,2,3)
plot(phi_offset*180/pi,Ir,phi_offset*180/pi,Qr); title('Reflected
in phase and quadature components of comon mode error signal')
subplot(2,2,2) plot(phi_offset*180/pi,abs(Ed).^2) title('Power at
dark port') subplot(2,2,4)
plot(phi_offset*180/pi,Id,phi_offset*180/pi,Qd);
```

```
title('Transmitted in phase and quadature components of comon mode
error signal')
```

C.2 Sub file

```
function [Ed,Er]=PRMtf(phi_p,phi_m,phi_d ,Ein,Es)
% This function calculates the dark fringe, reflected port and
% circulating fields as a function of the single pass phases
% and the Input Fields. All phases are zero on resonance.

global tbs rbs rp tp tm rml rms FWHM

%%%% Define Michelson ref/trans %%%%

rml=(tbs^2*exp(i*2*phi_d)+rbs^2.*exp(-i*2*phi_d)).*exp(i*2*phi_m);
    % [Eref/Ein]
rms=(tbs^2*exp(i*2*phi_d)+rbs^2.*exp(-i*2*phi_d)).*exp(i*2*phi_m);
    % [Eref/Ein]

%rms=-(tbs^2.*exp(-i*2*phi_d)+rbs^2.*exp(i*2*phi_d)).*exp(i*2*phi_m);
    % [Ed/Es]
tm=2*rbs.*tbs.*sin(2.*phi_d).*exp(i.*2.*phi_m);
    % [Eref/Es]

%%%% Cavity transfer functions %%%%

X=(1-rp*rml.*exp(i*2*phi_p));

Ed=Es*(rms+(tm.^2.*rp*exp(i*2*phi_p))./X)+Ein.*i*tp.*tm.*exp(i*phi_p)./X;
Er=Ein*(rp-(tp.^2.*rml*exp(i*2*phi_p))./X)+Es.*i*tp.*tm.*exp(i*phi_p)./X;
%%%%%%%%%%%%%%%%%%%%%%%%%%%%%%%%%%%%%%%%%%%%%%%%%%%%%%%%
```

Appendix D

Control Equipment

D.1 Servo frequency response

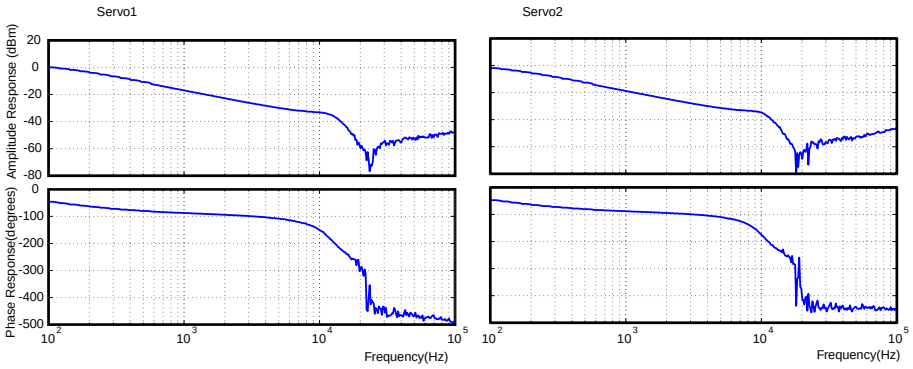

Figure D.1: Power recycling cavity and differential mode locking servos frequency response.

D.2 PZT response

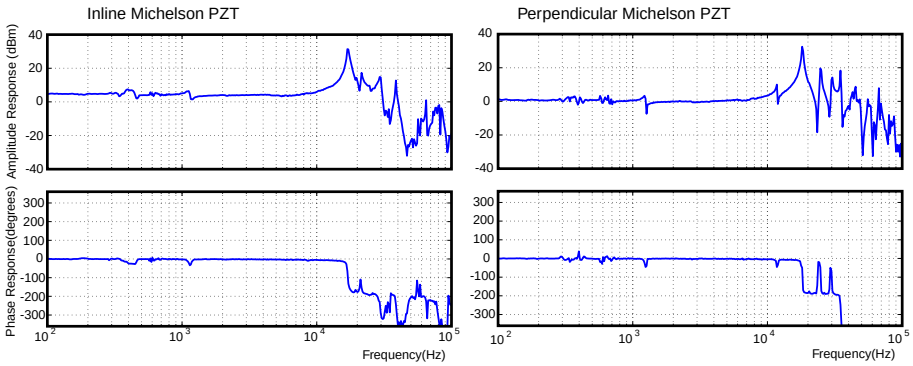

Figure D.2: The two Michelson arm mirror PZT amplitude and phase response.